

BICLUSTERING RANDOM MATRIX PARTITIONS WITH AN APPLICATION TO CLASSIFICATION OF FORENSIC BODY FLUIDS

BY CHIEH-HSI WU^{1,a} , AMY D. ROEDER^{2,b} AND GEOFF K. NICHOLLS^{3,c} 

¹*Mathematical Sciences, University of Southampton, ^ac-h.wu@soton.ac.uk*

²*Cellmark Forensic Services, ^baroeder@cellmark.co.uk*

³*Department of Statistics, University of Oxford, ^cnicholls@stats.ox.ac.uk*

Classification of unlabeled data is usually achieved by supervised learning from labeled samples. Although there exist many sophisticated supervised machine learning methods that can predict the missing labels with a high level of accuracy, they often lack the required transparency in situations where it is important to provide interpretable results and meaningful measures of confidence. Body fluid classification of forensic casework data is the case in point. We develop a new Biclustering Dirichlet Process (BDP), with a three-level hierarchy of clustering, and a model-based approach to classification which adapts to block structure in the data matrix. As the class labels of some observations are missing, the number of rows in the data matrix for each class is unknown. The BDP handles this and extends existing biclustering methods by simultaneously biclustering multiple matrices each having a randomly variable number of rows. We demonstrate our method by applying it to the motivating problem, which is the classification of body fluids based on mRNA profiles taken from crime scenes. The analyses of casework-like data show that our method is interpretable and produces well-calibrated posterior probabilities. Our model can be more generally applied to other types of data with a similar structure to the forensic data.

1. Introduction. Classification of body fluids in a forensic setting is concerned with identifying the type of body fluid present in specimens collected from a crime scene. One methodology used for body fluid identification is messenger RNA (mRNA) profiling (Harbison and Fleming, 2016). This technique assays samples for the presence of mRNA species (markers) that are characteristic of particular body fluids. The mRNA signal data is given as a sample/feature matrix, in which the rows are *mRNA profiles* for different specimens, and columns correspond to different mRNA markers. Matrix entries are binary indicators of marker presence/absence obtained by thresholding a marker amplification response measure (Lindenbergh et al., 2012; Akutsu et al., 2022) described below. Classification of unlabeled fluid-types using binary marker profiles is straightforward: if we simply choose the fluid-type with the most amplified target-markers (Table 5 in Appendix) reasonable accuracy can be obtained, though some classifications are ambiguous due to the presence of ties. However, the real challenge is to produce well-calibrated measures of uncertainty for the unknown true fluid-type of a given mRNA profile. In the following, we refer to “classifying profiles” as a shorthand for “quantifying the uncertainty in the assignment of unlabeled mRNA profiles to fluid-types”.

Likelihood ratios are commonly used in court (Morrison, 2021), so well-calibrated likelihood ratios have particular importance. Careful statistical modeling is usually necessary to achieve this goal. However, the signal for or against a given fluid-type is often quite strong, and several data sets of labeled training profiles (with known true fluid-types) are available

Keywords and phrases: Forensic body fluid analysis, biclustering, Dirichlet process, supervised classification, Bayesian inference, Cut-Models, MCMC.

and large enough for off-the-shelf machine learning methods, such as random forests and support vector machines (SVM), to be used for classification (Tian et al., 2020; Wohlfahrt et al., 2023). Bayesian model-based approaches include that of de Zoete, Curran and Sjerps (2016), using naïve Bayes, and the work of Fujimoto et al. (2019), involving fitting partial least squares-discriminant analysis. However, these methods do not accommodate heterogeneity in the sample population of mRNA profiles within a fluid-type. In order to model this heterogeneity, we cluster mRNA profiles within a fluid-type and cluster the mRNA marker signals targeting each particular fluid-type. This *biclustering* captures signal patterns in the sample and feature populations.

Matrix biclustering methods, which cluster samples and features simultaneously, are widely used in bioinformatics. In our setting and Li et al. (2020), samples in a row cluster share similar patterns over features, while feature clusters identify features that share similar patterns over samples within a given row cluster. The transpose of this setup, clustering samples within feature clusters, seems more common (see for example, Lee et al. (2013) and citing literature). This conditional biclustering is just one of many bicluster patterns which have found use: we list some of these and their many applications in our review below. In these applications, the goal of the inference is often the biclustering itself, though it also supports dimension-reduction for estimation of latent matrix-element parameters (Hochreiter et al., 2010; Murua and Quintana, 2022; Lee et al., 2013). Biclustering as a model supporting sample-classification seems to be less common.

In this paper, we present a new method for biclustering in Bayesian- and Cut-Model classification, which we call the Biclustering Dirichlet process over Random Row Partitions of Matrices (or BDP for short) and apply it to classify (apparent) single-source forensic mRNA profiles. Our clustering problem has a three-level hierarchy of clusters: within the highest level grouping that partitions profiles into fluid-types, we have fluid-subtype clusters; marker clusters are nested within the subtype clusters. Figure 1 displays the top two levels of the hierarchy, whereas Figure 2 displays the bottom two levels. In our training data, the assignment of profiles to fluid-types is fixed, as the fluid-type labels are known, so the fluid-types contain a “core” of labeled profiles. All body fluids tested were one of the five body fluids being targeted. However, the assignment of unlabeled mRNA profiles to fluid-types is unknown, so the set of profiles partitioned by the subtype clustering within a fluid-type includes a random subset of the unlabeled profiles: a model for random partitions of random sets of elements informs the ultimate fluid-type classification. This is a novel element of our work.

Markers (i.e., columns) come in fixed groups defined by the fluid-type they target; we call these *marker groups*. At the lowest level of biclustering, markers in each marker group are clustered within subtypes. This can be seen in Figure 2, which shows a possible biclustering of a fluid-type/marker-group *block*. This block represents one of the 25 blocks in the grid in Figure 1. Subtype clusters and marker clusters together define a biclustering of a row of these blocks, with a common subtype partition across all marker groups and independent marker-clustering of the markers in each marker group within each subtype. We call a row of the five blocks a *fluid-type matrix*, so in summary, we model independent nested biclustering of multiple fluid-type matrices, allowing a random assignment of unlabelled mRNA profiles to fluid-type matrices.

In the specific forensic setting of our application, each unlabeled profile would be classified one-at-a-time and independently of other unlabeled profiles for legal and ethical reasons. This restriction does not apply in other application domains, so we equip our notation in sections 3, 5, 6 and 7 to handle joint classification of multiple unlabeled profiles.

The models and computational methods that we set up here are motivated by our forensic data and can be applied to other types of forensic data for body fluid classification, such as protein (Legg et al., 2014) and microRNA markers (Fujimoto et al., 2019; He et al., 2020).

However, they may be useful for supervised classification more generally: class labels group labeled feature vectors into separate matrices, in which feature vectors in the same class are rows; classifying the unlabeled feature vectors amounts to assigning unlabeled feature vectors as new rows into one of the class matrices; biclustering with the BDP will be useful if the features in each class matrix have a subgroup structure, which varies across subgroups of the feature-vectors. This works if the class label is a categorical response and the features are covariates, or the class label is a categorical covariate and the features are conditionally independent response values. It is helpful if the number of features is relatively small (less than about 10) or comes in fixed groups (like our marker groups) of relatively small size, and latent matrix parameters can be integrated analytically. If this is not the case, then our BDP-classification scheme may be a useful joint model for biclustering and classification. However, our MCMC scheme would need to be extended to handle Monte Carlo integration over latent parameters and column clustering via Monte Carlo, along the lines of [Lee et al. \(2013\)](#) and [Li et al. \(2020\)](#), but with additional updates allowing rows to move from one matrix to another.

1.1. Our contribution. We take the (transpose of the) “NoB-LoC” biclustering process ([Lee et al., 2013](#)) as our starting point for model elaboration. Each matrix cell has one or more latent parameters. Our biclustering model groups these parameters across cells; all parameters in a bicluster are equal. This is not the case in NoB-LoC, so we first modify the distribution of parameters within biclusters and arrive at a model like the BAREB model ([Li et al., 2020](#)) for periodontal data. Those authors had a two-level biclustering hierarchy and used a multinomial-Dirichlet distribution to define the distribution over clusterings at both levels. We use the closely related Dirichlet Process (DP, [Ferguson \(1973\)](#)) and Multinomial Dirichlet Process (MDP, [Ghosal and van der Vaart \(2017\)](#)). The change is detailed in Section 4.2.

The data matrix, to which we apply biclustering, consists of 25 sub-matrix blocks arranged in a five-by-five grid. Each horizontal band of five sub-matrices, making up a row of blocks, gives all the data for one fluid-type. The biclustering is performed on each block but needs to be correlated along the blocks within a fluid-type and yet independent from one fluid-type to another. The BDP meets this requirement by forming a product of biclusterings over fluid-type matrices.

Our inferential goal is to identify the fluid-type of an unlabeled profile. The fluid-type of a profile is uncertain, so unlabeled profiles move between fluid-types in our Monte-Carlo. In the target posterior distribution, the set of rows partitioned by the BDP for a given fluid-type is random, as it depends on which unlabeled profiles are assigned to that fluid-type. BDP also extends the product of biclustering to randomly partition random sets of profiles, which is our main novel contribution to the biclustering methodology.

Fitting a BDP is challenging, as each partition of the high-level clustering has an associated realisation of a DP, like NoB-LOC and BAREB. In NoB-LoC and citing literature, this is handled using carefully adapted reversible jump proposals. However, in our specific setting, we can integrate out all parameters of the BDP below the subtype-clustering exactly; this leaves us with a marginal posterior defined on partitions of the rows of the fluid-type matrices. This is just what we need, as our inferential goal is to locate unlabeled profiles within fluid-types, so it is not of interest to estimate the values of latent parameters or the full biclustering itself. It also allows straightforward Markov Chain Monte-Carlo (MCMC) simulation.

Finally, a user can obtain a well-calibrated posterior probability for the unknown fluid-type of an mRNA binary profile, and this answers the application problem. We use a training data set for model development and apply it to classification on a test set. We show that the posterior probabilities obtained for class labels are well-calibrated, in the sense that Beta-calibration ([Kull, Filho and Flach, 2017](#)) gives recalibrated class probabilities which are close to the original posterior probabilities.

1.2. *Previous work on forensic body-fluid classification.* We divide work on body-fluid identification into two categories. The first aims to verify whether a sample is of a specific fluid-type, such as the work by [Akutsu et al. \(2020\)](#), where they present a multiplex RT-PCR assay, i.e., a small set of mRNA markers (ESR1, SERPINB13, KLK13, CYP2B7P1, and MUC4) and estimate a likelihood ratio using Bayesian inference.

The second category classifies the sample as one of a finite number of candidate fluid-types, as here. [He et al. \(2020\)](#) use discriminant analysis with forward stepwise selection to classify a micro RNA (miRNA) profile into one of five fluid-types of interest (peripheral blood, menstrual blood, vaginal secretion and semen), and [Tian et al. \(2020\)](#) used a random forest to classify DNA methylation profiles to venous blood, menstrual blood, vaginal fluid, semen and buccal cells, while [Jacob, Fürst and Hadrys \(2019\)](#) also uses a random forest to classify mRNA profiles. Bacterial community composition data has also been used to predict body fluid-types: ([Wohlfahrt et al., 2023](#)) use a support vector machine and tree-ensemble methods and reliably distinguish between CVF and MTB, a challenge for mRNA molecular data. While these authors all demonstrate accurate prediction with their model, they do not attempt to quantify uncertainty in-class assignments.

Methods suitable for samples which contain a mixture of different fluid-types have also been developed ([Akutsu et al., 2022](#)). Among these [Ypma et al. \(2021\)](#) treat mixtures using neural nets and random forest analysis in a frequentist setting and uses a form of Platt scaling ([Platt, 2000](#)) to calibrate likelihood ratios. Their choice of covariate makes their Platt-scaling resemble Beta-scaling. Further details on data types used for body fluid identification are discussed in [Sijen \(2015\)](#).

1.3. *Previous work on biclustering.* The “NoB-LoC method” ([Lee et al., 2013](#)) is a model for biclustering with a nested structure. It is applied to protein expression level data from breast cancer patients. The method identifies subgroups of proteins (columns there) and then clusters the samples (rows in that setting) within each protein subgroup to give biclusters: within each bicluster, parameters are shared across samples but not across proteins. In the work ([Zuanetti et al., 2018](#)) involving the related Nested Dirichlet Process (NDP, [Rodríguez, Dunson and Gelfand \(2012\)](#)), this parameterization is called a “marginalized” NDP because the DP-realizations are integrated out. [Zuanetti et al. \(2018\)](#) used NoB-LoC to identify clusters of DNA mismatch repair genes based on their gene-gene interactions and those of microRNA based on bind strength across different genes.

[Xu et al. \(2013\)](#) and [Zanini \(2019\)](#) build on [Lee et al. \(2013\)](#): [Xu et al. \(2013\)](#) gives a non-parametric Bayesian local clustering Poisson model (NoB-LCP) to infer the biclustering of histone modifications and genomic locations; [Zanini \(2019\)](#) extends NoB-LoC to handle protein expression data from lung cancer patients to identify clusters of proteins and the clusters of patients and cell lines nested therein. Like NoB-LoC, the parameters θ are independent across columns within a bicluster.

[Li et al. \(2020\)](#) work in a similar setting to [Lee et al. \(2013\)](#). One important difference is that the entries in the matrix that they bicluster are covariates in a linear model with an independent response for each matrix row. The model effect-values associated with each cell are identified in each bicluster. [Yan et al. \(2022\)](#) is similar in that they bicluster a matrix of covariate-values in a model for a row-response. They carry out variable selection within each row partition of the HapMap genomic SNP data, which means that they are selecting different effects for different groups of individuals. These two papers contrast much of the work that we have found, where matrix entries are response values. [Li et al. \(2020\)](#) take a Multinomial-Dirichlet *Distribution* (MDD) with J categories for both row and nested column partitions. This prior, often used for clustering in mixture models, allows empty partition sets;

the distribution over occupied sets is essentially the MDP (the parameters α_i in the Dirichlet-distribution must be set to $\alpha_i = \alpha/J$, for all $i \in \{1, \dots, J\}$ to get the MDP. Their “BAREB-model” has biclusters distributed like NoB-LoC but is closer to our BDP setup as there is one independent parameter associated with each bicluster (compare Figure 1 in Li et al. (2020) and Figure 2 above). They applied their model to the analysis of biomedical dental features measured across tooth-sites and over patients, selecting upper bounds on the number of clusters using the WAIC (Watanabe, 2012; Vehtari, Gelman and Gabry, 2017). Like many of the papers developing NoB-LoC for new applications, BAREB-analysis uses Reversible-Jump MCMC to fit the model to data. The ultimate goal of the inference in BAREB is to estimate effect sizes in a regression model with different parameters for each bicluster, though the biclusters themselves are also of interest. The goal of our work is to classify unlabeled profiles, and this makes the most important difference between our work and BAREB and NOB-LoC: the number of rows in each matrix we bicluster is random, as the matrix to which an unlabeled profile belongs is unknown. Additionally, a key conceptual difference between BAREB and our method is in the assignment of the covariates and the response. In BAREB, entries in the biclustered matrix are covariate values informing a response y . In contrast, entries in our profile matrix \mathbf{X} are multivariate response values: the fluid-type y is the covariate. This is natural in our setting, as the fluid type of a sample determines mRNA marker amplification. However, this difference is not material for the biclustering model itself.

There are several other Bayesian non-parametric methods for biclustering, taking different biclustering patterns across the target matrix. In VariScan (Guha and Baladandayuthapani, 2016) the column clustering is conditioned on the row clustering, but there is no independent DP within each row-cluster (as we read Equation 2.2 in that work). This allows cells in different row clusters to be assigned to the same bicluster. Different prior biclustering distributions are appropriate in different applications. The object of many biclustering analyses is to group exchangeable response values in different matrix cells into biclusters. Different patterns of biclustering, as in VariScan, NoB-LoC and BNP reflect different prior expectations about the properties of these exchangeable groups.

Guha and Baladandayuthapani (2016) elicit a Poisson-Dirichlet-Process (PDP, Perman, Pitman and Yor (1992)) prior for distributions over row partitions in VariScan. The motivating application in this group of papers is high-throughput gene-expression profile data over patients. We take the simpler Multinomial-Dirichlet-Process (MDP) as our prior for row partitions for similar reasons: it captures our prior expectations about the number and distribution of row- and column-partitions. The upper bound J , introduced in Section 4.1 below, on the number of clusters in our MDP is a prior hyperparameter. If we gave J a Poisson hyperprior, we would have a PDP.

Jha (2018) extends VariScan to mixed data types. Zhang et al. (2019) takes the VariScan bicluster structure, in which biclusters can cross row clusters, but replaces the PDP partition prior with an MDD prior of the type used by Li et al. (2020), using a grid search to find a good choice of upper bounds on the numbers of row and column clusters.

In other related work Ren et al. (2020) cluster time-series data for blood pressure over time and across patients. Considering each time-series as a matrix-row, they take a DP over row partitions and then partition the time-series within a row cluster serially, using a change-point process to identify partition boundaries.

We have focused on Bayesian non-parametric methods, in which the column clustering is nested in, or at least conditional on, the row-clustering. However, early parametric bi-clustering (Meeds and Roweis, 2007) took independent Pitman-Yor partition priors on rows and columns creating a “plaid” biclustering in a checkerboard pattern without nesting. More recently, Murua and Quintana (2022) used a Bayesian plaid model with independent stick-breaking process priors on rows and columns to analyse datasets of histone modifications across genomic locations and gene expression data over time and across genes.

TABLE 1
Profile counts and the candidate markers for each body fluid-type in the training and test datasets.

Body fluid-type	Profile counts		Candidate Markers
	Train	Test	
Cervical fluid	59	24	CYP, HBD1, Lcris, Lgas, MUC4
Menstrual blood	31	0	Hs202072, LEFTY2, MMP10, MMP11, MMP7, MSX1, SFRP4
Saliva	80	10	HTN3, MUC7, PRB4, SMR3B, STATH
Blood	65	2	ALAS2, GlycoA, HBB, PF4, SPTB
Semen	86	10	MSMB, PRM1, PRM2, SEMG1, TGM4
Housekeeping	N/A	N/A	TEF, UCE

Many applications of biclustering in the bioinformatics literature use sparse factor-analysis (Hochreiter et al., 2010; Moran, Ročková and George, 2021; Wang and Stephens, 2021) in which biclustering sets are (possibly overlapping) rectangular subsets of the target sample/feature matrix (see for example Figure 3 in Moran, Ročková and George (2021)). FABIA (Hochreiter et al., 2010) is widely used for this purpose. Closely related to independent component analysis (ICA, Hyvärinen (1999)), it identifies biclusters in gene-expression data using factor-analysis with sparse loadings and factors. Sparsity is achieved using Laplace priors, while inference is carried out via variational EM to estimate MAP values for factor and loading matrices. This gives accurate point estimates but does not feed uncertainty into downstream inference. In Moran, Ročková and George (2021), sparsity is induced using Spike-and-Slab Lasso priors (Ročková and George, 2018) for factors and loadings. They identify subtypes of breast cancer from gene expression data and recover major cell types from scRNA expression-level data across cell types, using Bayesian inference to quantify uncertainty. Wang and Stephens (2021) presents a computational framework suitable for fitting very general sparse factorisation models, alternating between Empirical-Bayes estimation of prior hyper-parameters and Variational-Bayes (VB) approximation of parameters with the final VB posterior quantifying uncertainty.

2. mRNA profile data. Our data consist of 27 binary features measured on samples. Following laboratory processing, the presence/absence of each marker ($M = 27$) in a sample is visualized in an electropherogram that represents the level of detection of each marker as a peak height measured in relative fluorescence units. The markers listed in Table 1 were chosen to respond strongly or “light up” for a specific fluid-type. We have $F = 5$ body fluid-types, cervical fluid (1/CVF), menstrual blood (2/MTB), saliva (3/SLV), blood (4/BLD) and semen (5/SMN), and five groups of markers. The markers in each group target one of the fluid-types. A raw profile is converted to an M -dimensional binary marker profile using a cut-off threshold, such that an entry in a binary profile records the amplification status (above or below the threshold) of an mRNA marker in the raw profile. Details on how the data is generated can be found in Appendix B.

The goal of our analysis is to infer the fluid-type of an unlabeled binary profile. We work with two data sets: a training dataset with 321 profiles and a test dataset with 46. These data are summarised in Table 1. Roughly speaking the training data are gathered under “laboratory conditions,” while the test data are gathered under conditions much closer to casework scenarios. We expand on this in Appendix B and return to it in Section 6.1.

All our data are labeled as we know the fluid-type of all the profiles in both datasets. We used the training data for model development, using leave-one-out cross-validation (LOOCV) to check performance, where each training profile held-out is treated as unlabeled. Subsequently, we tested our methods by treating the profiles in the test dataset as unlabeled. The test data came to us later in our work, and we did not revise our methods after applying them to the training data, so the results we report on the test dataset are “first shot” and should be

representative of performance on new marker profiles drawn from the same sample population as the test data.

The training data are visualized in Figure 1: each row of Figure 1 gives the binary marker profile for a unique sample; each column gives the binary responses of a unique marker. Rows/profiles are grouped into the five fluid-types of the sample labels, and columns/markers are grouped by the fluid-type they target, giving the 25 blocks. The binary profiles in the training data show heterogeneity in marker patterns, and in particular, there appear to be subtypes within fluid-types. We have colored the markers to highlight a possible subtype grouping obtained using k -means clustering on rows within each fluid-type. This may reflect some sort of structure in the population from which the samples are drawn. Our analysis must take this unknown subtype structure into account.

3. Observation model. Suppose we have T profiles from samples with known fluid-type (labeled profiles) and U unlabeled profiles for $N = T + U$ in total. Let $\mathcal{N} = \{1, \dots, N\}$, $\mathcal{M} = \{1, \dots, M\}$ and $\mathcal{F} = \{1, \dots, F\}$ denote the profile, marker and fluid-type index-sets. \mathcal{M}_g represents the index-set for markers targeting body-fluid-type $g \in \mathcal{F}$, so that $(\mathcal{M}_1, \dots, \mathcal{M}_F)$ is a partition of \mathcal{M} , and $M_g = |\mathcal{M}_g|$ is the number of markers targeting fluid-type $g \in \mathcal{F}$ (seven for MTB and otherwise five).

Denote by $\mathbf{Y} = (y_1, \dots, y_N)$ a vector of class labels with $y_i \in \mathcal{F}$ for $i \in \mathcal{N}$ giving the fluid-type for the i th observation. Suppose y_i is known for $i \in \mathcal{T} = \{1, \dots, T\}$ and unknown for $i \in \mathcal{U} = \{T + 1, \dots, T + U\}$. Our aim is to infer the missing fluid-type labels y_i , $i \in \mathcal{U}$ using their binary mRNA marker profiles $x_i = (x_{i,1}, \dots, x_{i,M})$ as feature vectors and training on the labeled data (y_i, x_i) , $i \in \mathcal{T}$. Let $\mathbf{X} = (x_{i,j})_{i \in \mathcal{N}}^{j \in \mathcal{M}}$ be a $N \times M$ binary matrix, with a marker profile $x_i \in \{0, 1\}^M$ in each row. In the saturated model

$$(1) \quad x_{i,j} \sim \text{Bernoulli}(\theta_{i,j}),$$

are conditionally independent, given $\theta = (\theta_{i,j})_{i \in \mathcal{N}}^{j \in \mathcal{M}}$ with $\theta_{i,j} \in [0, 1]$ for all $i \in \mathcal{N}$, $j \in \mathcal{M}$.

We reparameterize the missing fluid-type variables $\mathbf{Y}_{\mathcal{U}} = (y_i)_{i \in \mathcal{U}}$. Let

$$(2) \quad \mathcal{V}_f(\mathbf{Y}_{\mathcal{U}}) = \{i \in \mathcal{U} : y_i = f\}$$

be the indices of all the unlabeled profiles assigned by some choice of $\mathbf{Y}_{\mathcal{U}} \in \mathcal{F}^{\mathcal{U}}$ to fluid-type $f \in \mathcal{F}$. We call the vector, $\mathcal{V} = (\mathcal{V}_1, \dots, \mathcal{V}_F)$, an “assignment partition” of profiles in \mathcal{U} as $\mathcal{V}_f \subseteq \mathcal{U}$ is the set of unlabeled profiles that are assigned to fluid-type f . The sets in \mathcal{V} are ordered and may be empty: for example, $\mathcal{V} = (\{1, 2\}, \emptyset, \dots, \emptyset)$ and $\mathcal{V}' = (\emptyset, \dots, \emptyset, \{1, 2\})$ are different assignment partitions. We work with \mathcal{V} and map back to $\mathbf{Y}_{\mathcal{U}}$ at the end using $y_i(V) = \{f \in \mathcal{F} : i \in \mathcal{V}_f\}$.

Let $\mathcal{T}_f = \{i \in \mathcal{T} : y_i = f\}$ be the indices of labeled data in fluid-type $f \in \mathcal{F}$, and let $\mathcal{N}_f = \mathcal{T}_f \cup \mathcal{V}_f$ represent the $N_f = |\mathcal{N}_f|$ profile-indices labeled or assigned by \mathcal{V} to be in fluid-type f . The sub-matrix $\mathbf{X}_f = [x_{i,j}]_{i \in \mathcal{N}_f}^{j \in \mathcal{M}}$ is the $N_f \times M$ fluid-type matrix of observations on fluid-type f . The full observation model is

$$(3) \quad \begin{aligned} p(\mathbf{X}|\theta) &= \prod_{f \in \mathcal{F}} p(\mathbf{X}_f|\theta, \mathcal{V}) \\ &= \prod_{f \in \mathcal{F}} \prod_{g \in \mathcal{F}} \prod_{i \in \mathcal{N}_f} \prod_{j \in \mathcal{M}_g} \theta_{i,j}^{x_{i,j}} (1 - \theta_{i,j})^{1-x_{i,j}}, \end{aligned}$$

where conditioning on \mathcal{V} is needed to fix the profiles $i \in \mathcal{N}_f$ assigned to fluid-type $f \in \mathcal{F}$.

Our ultimate goal is to estimate \mathcal{V} using the posterior $\pi(\mathcal{V}|\mathbf{X})$, integrating over uncertainty in θ and any other latent variables. In the next section, we give a prior model for the parameters θ .

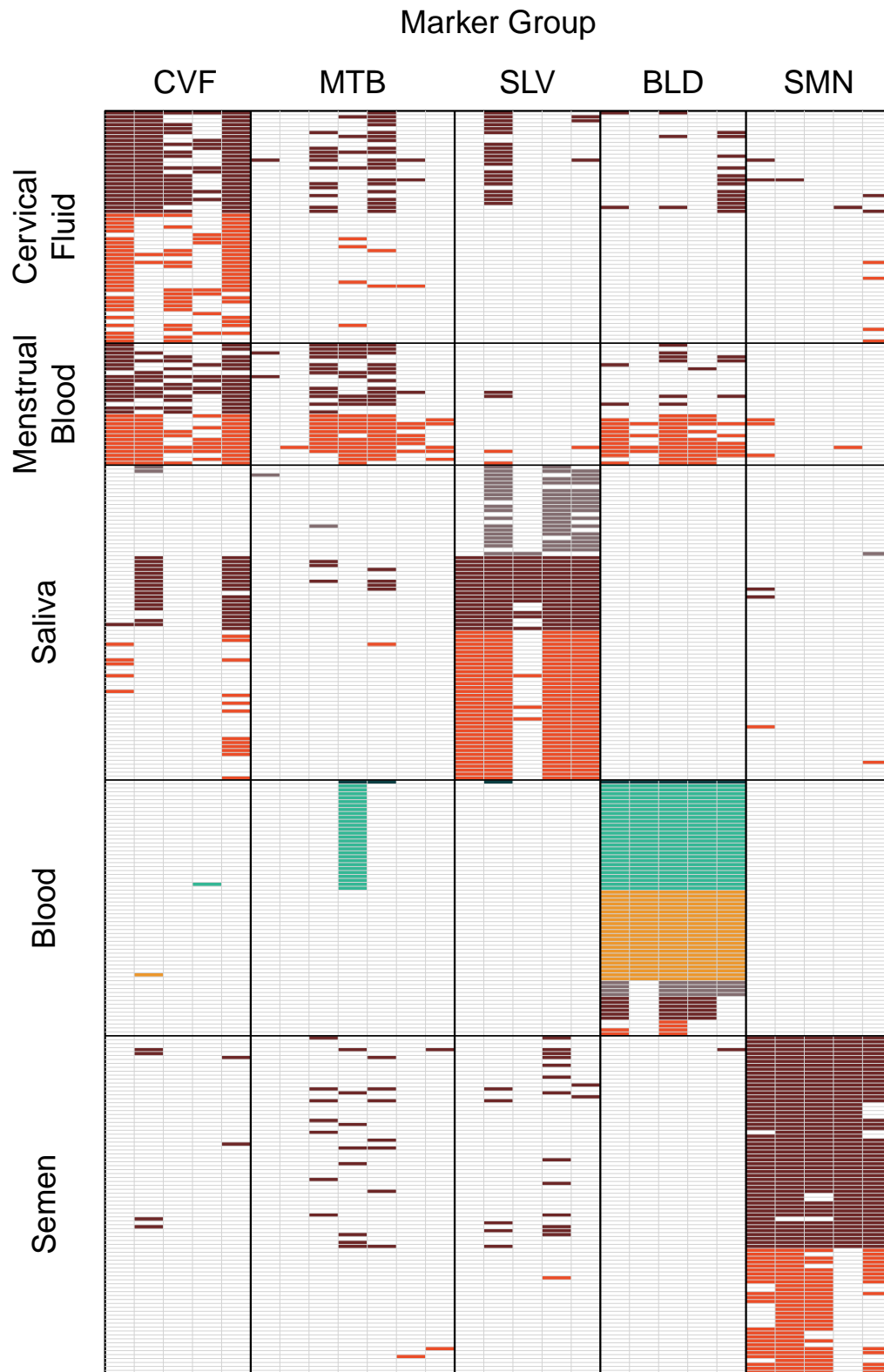


FIG 1. RNA profiles of the training set, colored by row subtype (*k*-means) within fluid-type.

4. Biclustering prior. Here, we set out the BDP distribution over parameters and bi-clusters. For comparison with earlier work on NoB-LoC and clarity of exposition, we first specify the process on a single fluid-type/marker group matrix: that is the setting for earlier work. We then specify the process on a fluid-type matrix (i.e., across multiple marker-group blocks). Finally, we take a simple product of fluid-type matrix biclusterings to get the BDP. In this section, the assignment of profiles to fluid-types is fixed. In Section 5, we will allow for uncertainty in the assignment of unlabeled profiles to fluid-types when the “row-content” of each fluid-type matrix is random.

4.1. Multinomial Dirichlet Process. The Dirichlet Process (DP) and the associated Chinese Restaurant Process (CRP) are projective models for partitions. However, in order to avoid the tail of small clusters seen in the CRP, we work with a *Multinomial Dirichlet Process* (MDP), which sets an upper bound on the maximum number of partition sets. The MDP converges (rapidly in our experience) to the DP as this bound is taken to infinity. See Ghosal and van der Vaart (2017) for further discussion.

Given $A \in \mathbb{N}$, let Ξ_A^J be the set of all partitions of $A = \{1, \dots, A\}$ into at most J sets. Suppose $Q \sim \text{MDP}(\alpha, H; J)$ is a generic MDP with size parameter $\alpha > 0$, base distribution H , and the maximum number of clusters $J \geq 1$. If $\psi_i \stackrel{\text{iid}}{\sim} Q$ for $i \in \{1, \dots, A\}$, then $\psi = \{\psi_1, \dots, \psi_A\}$ is equivalently given by taking a random partition $P \sim P_{\alpha, J}(\cdot)$ from the distribution over Ξ_A^J given in Equation 4 below, simulating parameters $\psi_k^* \sim H$ independently for all $k \in \{1, \dots, K\}$ and setting $\psi_i = \psi_{k_i}^*$ with $k_i = \{k : i \in P_k\}$, similar to the DP.

Let $P \sim \text{MCRP}(\alpha, J; A)$ be the multinomial “CRP” associated with $\text{MDP}(\alpha, H; J)$. The probability for partition $P \in \Xi_A^J$ is

$$(4) \quad P_{\alpha, J}(P) = \frac{\Gamma(\alpha)}{\Gamma(\alpha/J)^K} \frac{J!}{(J-K)!} \frac{\prod_{k=1}^K \Gamma(\alpha/J + |P_k|)}{\Gamma(\alpha + A)} \mathbb{I}_{K \leq J},$$

where $|P_k|$ is the number of elements in cluster $k \in \{1, \dots, K\}$, and the indicator function $\mathbb{I}_{K \leq J}$ evaluates to 1 if $K \in \{1, \dots, J\}$ and 0 otherwise. This distribution can be simulated by a process-of-arrivals like the CRP, so it is projective, and the simulation can be achieved by Gibbs sampling. However, we use Metropolis-Hastings updates, so Equation 4 is sufficient.

We emphasize that the MDP is not taken for computational convenience but on subjective grounds following elicitation. Replacing the MDP with the DP leads to some simplification; all the marginals derived below are still tractable. In later sections, we experiment with DP-like priors (large J) and find performance on the test set worsens slightly, so our choice is supported.

4.2. Biclustering a single matrix. The notation in this sub-section is set up for biclustering a single fluid-type/marker group matrix for clarity of exposition. It holds for this section and Appendix C only. In later sections, we expand the model to handle a grid of sub-matrices. The literature cited here typically partitions columns first and then rows within columns, i.e., the row-clustering is nested within column clusters. In the following, we use the terminology for our setting, where we cluster columns within row-clusters.

The value $x_{i,j} \in \{0, 1\}$ in cell $(i, j) \in \mathcal{N} \times \mathcal{M}$ has an observation model $x_{i,j} \sim p(\cdot | \theta_{i,j})$ with parameter $\theta_{i,j} \in [0, 1]$, conditionally independent within each cell. Insight gathered from the training data informs the prior for the θ -parameters. The rows of the training data in Figure 1 have been sorted and colored to highlight a potential row-clustering of profiles suggesting a group structure in the population of sample profiles. We term row-clusters within a fluid-type $f \in \mathcal{F}$ the subtypes of f : rows within a subtype have similar marker profile patterns, like a barcode. However, the subtype grouping is unknown: the coloring in Figure 1

(1,1)	(1,2)	(1,2)	(1,3)	(1,2)
(1,1)	(1,2)	(1,2)	(1,3)	(1,2)
(1,1)	(1,2)	(1,2)	(1,3)	(1,2)
(1,1)	(1,2)	(1,2)	(1,3)	(1,2)
(1,1)	(1,2)	(1,2)	(1,3)	(1,2)
(2,1)	(2,1)	(2,2)	(2,1)	(2,3)
(2,1)	(2,1)	(2,2)	(2,1)	(2,3)
(2,1)	(2,1)	(2,2)	(2,1)	(2,3)
(3,1)	(3,2)	(3,2)	(3,3)	(3,1)
(3,1)	(3,2)	(3,2)	(3,3)	(3,1)

FIG 2. A possible biclustering of a single matrix. Cells with the same color are in the same bicluster. The text within cells gives the (r, s) bicluster label, with $r \in \{1, \dots, K\}$ giving the row cluster label in the row partition $R = (R_1, \dots, R_K)$ of $\{1, \dots, N\}$, and $s \in \{1, \dots, K_r\}$ giving the column cluster label in the partition $S_r = (S_{r,1}, \dots, S_{r,K_r})$ of $\{1, \dots, M\}$.

only illustrates one of many plausible subtype groupings. Column clustering is applied separately to each marker group as markers in the same group are clearly correlated. In this case, columns in the same group have similar *proportions* of amplified markers rather than similar sequences. As we move from one (row) subtype to another, the column clustering changes. This suggests a nested clustering like BAREB (Li et al., 2020): cluster rows within fluid-type and columns within row subtypes; a bicluster is a group of matrix cells (i, j) in the same column-cluster of a row subtype; all cells (i, j) in a bicluster get the same $\theta_{i,j}$ -value.

Therefore, we use an MDP or a DP to partition the N rows into K sets $R = (R_1, \dots, R_K)$ with $R_k \subset \{1, \dots, N\}$ for all $k \in \{1, \dots, K\}$. Then, we partition the M columns within each row-cluster $r \in \{1, \dots, K\}$ into K_r sets $S_r = (S_{r,1}, \dots, S_{r,K_r})$ with $S_{r,c} \subset \{1, \dots, M\}$ for all $c \in \{1, \dots, M\}$, using an independent process for each row cluster. This process partitions the matrix entries into sets or “biclusters” $C_{r,s} = R_r \times S_{r,s}$; the union of the biclusters $C_{r,s}$ over all $r \in \{1, \dots, K\}$, and $s \in \{1, \dots, K_r\}$ is $\{1, \dots, N\} \times \{1, \dots, M\}$, the set of all matrix cell labels. A possible biclustering of a single 10×5 matrix is shown in Figure 2. This corresponds to one of the 25 blocks in the data-matrix in Figure 1.

We specify the biclustering prior in terms of the MDP or DP marginals for partitions, the Chinese Restaurant Processes (CRP) priors, $\pi_R(R)$ and $\pi_S(S_r)$, $r \in \{1, \dots, K\}$ given in Equation 4. BDP and NoB-LoC take CRPs, while BAREB uses a Multinomial-Dirichlet Distribution in a mixture model prior for partitions. This has the MDP as its marginal if it is correctly parameterized, and we integrate out empty partitions (Ghosal and van der Vaart, 2017). NoB-LoC differs from the BDP and BAREB in the way parameters are assigned to cells within biclusters. In the BDP and BAREB, we simply set $\theta_{i,j} = \theta_{r,s}^*$ for all $(i, j) \in C_{r,s}$, with $\theta_{r,s}^* \sim h(\cdot)$ and h the base prior in the overall nested DP. The BDP posterior for a single fluid-type/marker group sub-matrix can be written

$$\pi_{\text{BDP}}(\theta^*, R, S | \mathbf{X}) \propto \pi_R(R) \prod_{r=1}^K \pi_S(S_r) \prod_{s=1}^{K_r} h(\theta_{r,s}^*) \prod_{(i,j) \in C_{r,s}} p(x_{i,j} | \theta_{r,s}^*).$$

In contrast, NoB-LoC sets $\theta_{i,j} = \theta_{i,s}^*$ for each $j \in S_{r_i,s}$, where r_i is the row-cluster containing row i , so it shares $\theta_{i,s}^*$ across all columns $j \in S_{r_i,s}$ but not across different rows $i \in R_r$. Its posterior is

$$\pi_{\text{NoB-LoC}}(\theta^*, R, S | \mathbf{X}) \propto \pi_R(R) \prod_{r=1}^K \pi_S(S_r) \prod_{s=1}^{K_r} \prod_{i \in R_r} h(\theta_{i,s}^*) \prod_{j \in S_{r,c}} p(x_{i,j} | \theta_{i,s}^*).$$

For further details of the relations between the BDP, NoB-LoC, and the NDP, in terms of DP, see realizations, see Appendix C.

4.3. *The Biclustering Dirichlet Process.* The BDP defined in Section 4.2 was restricted to a single fluid-type/marker group sub-matrix. We now extend this to the setting with multiple fluid-types and marker groups. Here, all partitions in R and S pick up an additional fluid-type subscript $f \in \mathcal{F}$, and the partitions in S have an extra marker-group subscript, $g \in \mathcal{F}$. Examples of the objects defined below are given in Appendix D and displayed in Figure 6.

4.3.1. *Row clusters.* For each $f \in \mathcal{F}$, $R_f \in \Xi_{\mathcal{N}_f}^{J_f}$ denotes a partition $R_f = \{R_{f(1)}, \dots, R_{f(K_f)}\}$ of the row indexes $\mathcal{N}_f = \mathcal{T}_f \cup \mathcal{V}_f$ of \mathbf{X} , labeled or assigned by \mathcal{V} to fluid-type f , and R_f has $K_f \in \{1, \dots, J_f\}$ subsets, which we term “row subtypes”. Let α_f be the fluid-type specific size parameter, we take $R_f \sim \text{MCRP}(\alpha_f, J_f; \mathcal{N}_f)$, giving the prior probability distribution π_R for R_f as

$$(5) \quad \pi_R(R_f) = P_{\alpha_f, J_f}(R_f),$$

where $P_{\alpha_f, J_f}(R_f)$ is given in Equation 4. The sub-matrix

$$\mathbf{X}_{f(k)} = [x_{i,j}]_{i \in R_{f(k)}}^{j \in \mathcal{M}}$$

represent the data in the “band” of rows in subtype R_f .

4.3.2. *Column clusters within row clusters.* Now, we partition the columns \mathcal{M}_g of $\mathbf{X}_{f(k)}$ within each marker group $g \in \mathcal{F}$ independently within each row subtype $f(k)$. This partition is informed by the data

$$\mathbf{X}_{f(k),g} = [x_{i,j}]_{i \in R_{f(k)}}^{j \in \mathcal{M}_g},$$

in \mathbf{X} , where the columns in \mathcal{M}_g intersect the rows in $R_{f(k)}$. For marker group $g \in \mathcal{F}$, let $L_g \geq 1$ be the maximum number of column clusters permitted, and $\Xi_{\mathcal{M}_g}^{L_g}$ be the set of all possible column partitions without exceeding L_g clusters. Then, we define a column partition $S_{f(k),g} \in \Xi_{\mathcal{M}_g}^{L_g}$ of the columns in marker group g (within row subtype k of fluid-type f) as a random partition of \mathcal{M}_g into $K_{f(k),g} \leq L_g$ disjoint sets. This partition is written as

$$S_{f(k),g} = \{S_{f(k),g(1)}, \dots, S_{f(k),g(K_{f(k),g})}\},$$

such that “column subtype” $l \in \{1, \dots, K_{f(k),g}\}$ of row subtype $f(k)$ is indexed using the notation $(f(k), g(l))$, which serve as the basic bicluster label.

Our prior model for column-partitions of a marker type $g \in \mathcal{F}$ within a row subtype $f(k)$ is an MCRP with the size parameter $\beta_g > 0$, specific to the marker group, so that $S_{f(k),g} \sim \text{MCRP}(\beta_g, L_g; \mathcal{M}_g)$, and the prior distribution π_S for this column partition is

$$(6) \quad \pi_S(S_{f(k),g}) = P_{\beta_g, L_g}(S_{f(k),g}),$$

where again $P_{\beta_g, L_g}(S_{f(k),g})$ is given by substituting its parameters and argument into Equation 4.

4.3.3. *Biclusters.* Let $R = (R_f)_{f \in \mathcal{F}}$ be the list of row partitions for the different fluid-types (a “joint partition”). For $f \in \mathcal{F}$ and all $k \in \{1, \dots, K_f\}$, $S_{f(k)} = (S_{f(k),g})_{g \in \mathcal{F}}$ represents the list of column partitions within the row subtype $f(k)$. Let $S_f = (S_{f(k)})_{k=1}^{K_f}$ and $S = (S_f)_{f \in \mathcal{F}}$, so R, S define a partition of the cells $\mathcal{N} \times \mathcal{M}$ of \mathbf{X} .

Given R, S , and for all $f, g \in \mathcal{F}$, $k \in \{1, \dots, K_f\}$ and $l \in \{1, \dots, K_{f(k),g}\}$, let

$$C_{f(k),g(l)} = \{(i, j) \in \mathcal{N} \times \mathcal{M} : i \in R_{f(k)}, j \in S_{f(k),g(l)}\}$$

be the set of matrix cells in bicluster $(f(k), g(l))$. Let

$$\mathcal{C}_{f(k),g} = \bigcup_{l=1}^{K_{f(k),g}} \{(f(k), g(l))\}$$

be the label-set for biclusters partitioning the matrix cells of $R_{f(k)} \times \mathcal{M}_g$, and correspondingly $\mathcal{C}_{f,g} = \bigcup_{k=1}^{K_f} \mathcal{C}_{f(k),g}$ in fluid/marker block $\mathcal{N}_f \times \mathcal{M}_g$,

$$\mathcal{C}_f = \bigcup_{g \in \mathcal{F}} \mathcal{C}_{f,g}$$

for biclusters partitioning the cells $\mathcal{N}_f \times \mathcal{M}$ in fluid-type f and $\mathcal{C} = \bigcup_{f \in \mathcal{F}} \mathcal{C}_f$ for all biclusters of $\mathcal{N} \times \mathcal{M}$.

4.3.4. Bicluster parameters. All mRNA markers $j \in \mathcal{M}_g$ of marker type $g \in \mathcal{F}$ are selected to be amplified in fluid samples $i \in \mathcal{N}_f$, when $f = g$, so we expect $\theta_{f(k),g(l)}^*$ to be large when $f = g$. However, some markers are known to be unreliable indicators and fail to be amplified for “their” target fluid-type. This is apparent in the data (Figure 1). Some off-diagonal blocks show a strong response for an off-target fluid-type (for example, in the MTB profiles, the CVF and BLD markers are frequently amplified). Therefore, to each bicluster $(f(k), g(l)) \in \mathcal{C}_{f(k),g}$ a parameter, we apply the prior

$$\theta_{f(k),g(l)}^* \sim \text{Beta}(a_{f,g}, b_{f,g}),$$

with potentially different hyper-parameters $a_{f,g} > 0$ and $b_{f,g} > 0$, and hence difference priors in each (f, g) -block. Fixed values for the prior hyper-parameters $a_{f,g}$ and $b_{f,g}$ are elicited using the training data in Appendix E).

Let

$$\theta_f^* = (\theta_{f(k),g(l)}^*)_{f(k),g(l) \in \mathcal{C}_f}$$

be the set of all base parameters for partitions in fluid-type f , and let $\theta^* = (\theta_f^*)_{f \in \mathcal{F}}$ be the set of all base parameters.

The base parameters θ^* are mapped to the original parameters by

$$\theta_{i,j} = \theta_{i,j}(\theta^*, R, S),$$

where, for $(i, j) \in \mathcal{N} \times \mathcal{M}$,

$$(7) \quad \theta_{i,j}(\theta^*, R, S) = \theta_{f(k),g(l)}^*, \quad \text{for all } (i, j) \in C(f(k), g(l)).$$

5. The Biclustering Posterior Distribution. In this section, we set out the posterior for the partition \mathcal{V} assigning unlabeled profiles to fluid-types. The only result used for later analysis is given in Section 5.3.2. We lead up to this by developing notation on simpler special cases. We begin by giving the likelihood contribution of a single bicluster cell.

5.1. Likelihood. The data $\mathbf{X}_{f(k),g(l)} = [x_{i,j}]_{(i,j) \in C_{f(k),g(l)}}$ in a single bicluster are Bernoulli random variables with a common parameter $\theta_{f(k),g(l)}^* \in [0, 1]$. Given the parameters and partition (θ^*, R, S) the observation model in Equation 3 is

$$x_{i,j} \sim \text{Bernoulli}(\theta_{i,j}(\theta^*, R, S)), \text{ jointly independent for } (i, j) \in \mathcal{N} \times \mathcal{M}$$

with $\theta_{i,j}(\theta^*, R, S)$ given in Equation 7.

The likelihood for the mRNA profile of observations in a given fluid-type $f \in \mathcal{F}$, row subtype $k \in \{1, \dots, K_f\}$, marker type $g \in \mathcal{F}$ and marker subtype $l \in \{1, \dots, K_{f(k),g}\}$ is

$$\begin{aligned}
 p(\mathbf{X}_{f(k),g(l)} | \theta_{f(k),g(l)}^*, R_{f(k)}, S_{f(k),g(l)}) &= \prod_{i \in R_{f(k)}} \prod_{j \in S_{f(k),g(l)}} p(x_{i,j} | \theta_{i,j}^*) \\
 (8) \quad &= \prod_{(i,j) \in C_{f(k),g(l)}} (\theta_{f(k),g(l)}^*)^{x_{i,j}} (1 - \theta_{f(k),g(l)}^*)^{1-x_{i,j}} \\
 (9) \quad &= (\theta_{f(k),g(l)}^*)^{s_{f(k),g(l)}} (1 - \theta_{f(k),g(l)}^*)^{c_{f(k),g(l)} - s_{f(k),g(l)}},
 \end{aligned}$$

where

$$s_{f(k),g(l)} = \sum_{(i,j) \in C_{f(k),g(l)}} x_{i,j}$$

is the number of 1's in $\mathbf{X}_{f(k),g(l)}$, and

$$c_{f(k),g(l)} = |C_{f(k),g(l)}|$$

is the number of cells $(i,j) \in C_{f(k),g(l)}$ in bicluster $(f(k), g(l))$.

5.2. Biclustering with a fixed assignment of unlabeled profiles to fluid-types. We now give the posterior for the joint distribution of row-partitions of multiple fluid-types. The assignment of unlabeled profiles to fluid-types is fixed. This joint distribution is a simple product of the posteriors for the individual fluid-types, so we begin by giving the marginal posterior for row-partitions of a single fluid-type with a fixed assignment partition.

5.2.1. Biclustering a single fluid-type with a fixed assignment partition. Suppose the assignment partition \mathcal{V} of unlabeled profiles $i \in \mathcal{U}$ to fluid-types is fixed, so for $f \in \mathcal{F}$ the rows in \mathcal{N}_f , and hence the set of elements partitioned by R_f , is fixed. The posterior distribution of the parameters θ_f^*, R_f, S_f associated with fluid-type f , given all data for fluid-type f , is

$$\begin{aligned}
 \pi(\theta_f^*, R_f, S_f | \mathbf{X}_f) &\propto \pi_R(R_f) \prod_{k=1}^{K_f} \prod_{g \in \mathcal{F}} \pi_S(S_{f(k),g}) \\
 (10) \quad &\times \prod_{l=1}^{K_{f(k),g}} h_{f,g}(\theta_{f(k),g(l)}^*) p(\mathbf{X}_{f(k),g(l)} | \theta_{f(k),g(l)}^*, R_{f(k)}, S_{f(k),g(l)}),
 \end{aligned}$$

where $\pi_R(\cdot)$ and $\pi_S(\cdot)$ are given in Equations 5 and 6, and $h_{f,g}$ is the density of a Beta($a_{f,g}, b_{f,g}$) distribution for fixed values of $a_{f,g}$ and $b_{f,g}$ elicited in Appendix E. As the prior $h(\cdot)$ is conjugate to the Bernoulli likelihood, the amplification probabilities $\theta_{f(k),g(l)}^*$ can be integrated out. Given

$$B(a_{f,g}, b_{f,g}) = \frac{\Gamma(a_{f,g})\Gamma(b_{f,g})}{\Gamma(a_{f,g} + b_{f,g})},$$

which is the Beta-function normalization of the Beta-prior in block (f, g) , and we obtain

$$\pi(R_f, S_f | \mathbf{X}_f) \propto \pi_R(R_f) \prod_{k=1}^{K_f} \prod_{g \in \mathcal{F}} \pi_S(S_{f(k),g}) \prod_{l=1}^{K_{f(k),g}} p(\mathbf{X}_{f(k),g(l)} | R_{f(k)}, S_{f(k),g(l)}),$$

where

$$(11) \quad p(\mathbf{X}_{f(k),g} | R_{f(k)}, S_{f(k),g}) = \prod_{l=1}^{K_{f(k),g}} p(\mathbf{X}_{f(k),g(l)} | R_{f(k)}, S_{f(k),g(l)}),$$

and

$$p(\mathbf{X}_{f(k),g(l)} | R_{f(k)}, S_{f(k),g(l)}) = \prod_{l=1}^{K_{f(k),g}} \frac{B(a_{f,g} + s_{f(k),g(l)}, b_{f,g} + c_{f(k),g(l)} - s_{f(k),g(l)})}{B(a_{f,g}, b_{f,g})}.$$

We further marginalize over partitions of the marker groups: we have $M_g = 5$ (for four marker groups $g = 1, 3, 4, 5$) and $M_g = 7$ (for $g = 2$). Summation over $S_{f(k),g} \in \Xi_{\mathcal{M}_g}^{L_g}$ is tractable because the number of partitions of five objects is 52 and 877 for seven. We have

$$(12) \quad \pi(R_f | \mathbf{X}_f) = \pi_R(R_f) \prod_{k=1}^{K_f} p(\mathbf{X}_{f(k)} | R_{f(k)}),$$

a posterior over $\Xi_{\mathcal{N}_f}^{J_f}$, in which

$$(13) \quad p(\mathbf{X}_{f(k)} | R_{f(k)}) = \prod_{g \in \mathcal{F}} p(\mathbf{X}_{f(k),g} | R_{f(k)}),$$

and

$$p(\mathbf{X}_{f(k),g} | R_{f(k)}) = \sum_{S_{f(k),g} \in \Xi_{\mathcal{M}_g}^{L_g}} \pi_S(S_{f(k),g}) p(\mathbf{X}_{f(k),g} | R_{f(k)}, S_{f(k),g}),$$

with $p(\mathbf{X}_{f(k),g} | R_f, S_{f(k),g})$ given in Equation 11. These marginalizations increase the efficiency of the MCMC as it eliminates the requirement to propose new column partitions $S_{f(K_f+1),g}$, $g \in \mathcal{F}$ when adding a row-cluster.

5.2.2. Biclustering multiple fluid-types with a fixed assignment partition. Assuming again that the assignment partition \mathcal{V} is fixed, the posterior distribution for the joint partition $R = (R_1, \dots, R_F)$ is simply the product,

$$(14) \quad \begin{aligned} \pi(R | \mathbf{X}) &= \prod_{f \in \mathcal{F}} \pi(R_f | \mathbf{X}_f) \\ &\propto \prod_{f \in \mathcal{F}} \pi_R(R_f) p(\mathbf{X}_f | R_f), \end{aligned}$$

with $R \in \Xi_{\mathcal{N}}^*$ the product space

$$\Xi_{\mathcal{N}}^* = \Xi_{\mathcal{N}_1}^{J_1} \times \Xi_{\mathcal{N}_2}^{J_2} \times \dots \times \Xi_{\mathcal{N}_F}^{J_F}$$

of joint partitions and $\pi(R_f | \mathbf{X}_f)$ given in Equation 12. No parameter is shared across fluid-types in this simple product of posteriors.

5.3. Biclustering with an unknown assignment of unlabeled profiles to fluid-types. This section first presents the prior and subsequently, the posterior for the joint distribution of row- and assignment partitions.

5.3.1. *Prior for assignment partitions of unlabeled profiles.* Recall the sets defined in Section 3: \mathcal{T} and \mathcal{U} are the index sets for labeled and unlabeled profiles respectively, and $\mathcal{V} = (\mathcal{V}_1, \dots, \mathcal{V}_F)$ is a partition of \mathcal{U} , giving the assignment of unlabeled profiles to fluid-types. Also, $\mathcal{T}_f = \{i \in \mathcal{T} : y_i = f\}$ is the set labeled profiles in fluid-type f , and $\mathcal{N}_f = \mathcal{T}_f \cup \mathcal{V}_f$ is the set of profiles labeled or assigned to fluid-type f . Let

$$\Xi_{\mathcal{T}, \mathcal{V}}^* = \Xi_{\mathcal{T}_1 \cup \mathcal{V}_1}^{J_1} \times \Xi_{\mathcal{T}_2 \cup \mathcal{V}_2}^{J_2} \times \dots \times \Xi_{\mathcal{T}_F \cup \mathcal{V}_F}^{J_F}$$

be the set of joint partitions $R = (R_1, \dots, R_F)$ given an assignment \mathcal{V} . If \mathcal{V} is fixed then $\mathcal{N}_f = \mathcal{T}_f \cup \mathcal{V}_f$ is fixed, and $\Xi_{\mathcal{T}, \mathcal{V}}^*$ and $\Xi_{\mathcal{N}}^*$ above are the same set. However, \mathcal{V} is now varying so, recalling $\mathcal{V} = \mathcal{V}(\mathbf{Y}_{\mathcal{U}})$ from Equation 2, let

$$\Psi_{\mathcal{U}} = \bigcup_{y_{\mathcal{U}} \in \mathcal{F}^{\mathcal{U}}} \{\mathcal{V}(y_{\mathcal{U}})\}$$

give the set of all assignment partitions, and finally, take

$$\Xi_{\mathcal{T}, \mathcal{U}}^* = \bigcup_{\mathcal{V} \in \Psi_{\mathcal{U}}} \Xi_{\mathcal{T}, \mathcal{V}}^*,$$

to be the set of all joint partitions, allowing for any assignment of the entries in \mathcal{U} to fluid-types. Any $R \in \Xi_{\mathcal{N}, \mathcal{U}}^*$ determines \mathcal{V} and hence $y_{\mathcal{U}}$, since

$$(15) \quad \mathcal{V}_f = \bigcup_{k=1}^{K_f} R_{f(k)} \cap \mathcal{U}$$

for $f \in \mathcal{F}$ and then $y_i = \{f \in \mathcal{F} : i \in \mathcal{V}_f\}$ for $i \in \mathcal{U}$.

We decompose the prior for R into the prior for $R|\mathcal{V}$ and a prior for \mathcal{V} , taking $\pi_{\mathcal{V}}(\mathcal{V}) = F^{-U}$, such that each $y_{\mathcal{U}} \in \mathcal{F}^{\mathcal{U}}$ is equally likely a priori. The prior for $R_f|\mathcal{V}_f$ is

$$R_f|\mathcal{V}_f \sim \text{MCRP}(\alpha_f, J_f; \mathcal{T}_f \cup \mathcal{V}_f),$$

as \mathcal{V}_f just determines the set \mathcal{N}_f that R_f is partitioning. Because $\{R\}$ and $\{R, \mathcal{V}\}$ are the same events,

$$\begin{aligned} \pi_R(R) &= \pi_{R, \mathcal{V}}(R, \mathcal{V}) \\ &= \pi_{\mathcal{V}}(\mathcal{V}) \prod_{f \in \mathcal{F}} \pi_R(R_f|\mathcal{V}_f) \\ &= F^{-U} \prod_{f \in \mathcal{F}} P_{\alpha_f, J_f}(R_f). \end{aligned}$$

5.3.2. *Posterior for assignment partitions of unlabeled profiles.* The joint posterior with missing fluid-types is then

$$\begin{aligned} \pi(R|\mathbf{X}) &= \pi(R, \mathcal{V}|\mathbf{X}) \\ &\propto \pi_{\mathcal{V}}(\mathcal{V}) \pi_R(R|\mathcal{V}) p(\mathbf{X}|R) \\ (16) \quad &= F^{-U} \prod_{f \in \mathcal{F}} \pi_R(R_f|\mathcal{V}_f) p(\mathbf{X}_f|R_f). \end{aligned}$$

Although this resembles Equation 14, here $R \in \Xi_{\mathcal{T}, \mathcal{U}}^*$, and therefore, the assignment \mathcal{V} of unlabeled profiles to fluid-types is a random (ordered) partition.

As an example of a quantity of interest, we might compute the marginal posterior probability for some unlabeled profile $i \in \mathcal{U}$ to have true fluid-type $y_i = f$, that is,

$$\Pr\{y_i = f|\mathbf{X}\} = \mathbb{E}_{R, \mathcal{V}|\mathbf{X}}(\mathbb{I}_{i \in \mathcal{V}_f}),$$

where the indicator function $\mathbb{I}_{i \in \mathcal{V}_f}$ evaluates to 1 if $i \in \mathcal{V}_f$ and 0 otherwise. This is estimated using MCMC targeting $\pi(R, \mathcal{V}|\mathbf{X})$.

5.3.3. Missing data. If some marker data values $x_{i,j}$ are missing, then they will be omitted from the product in Equation 8. In that case, $c_{f(k),g(l)}$ is the number of non-missing cells in $C_{f(k),g(l)}$, and the sum giving $s_{f(k),g(l)}$ runs over non-missing cells. The datasets used in this study have no missing values. Missing marker data are discussed further in Section G, where we prove that the posterior distribution of a profile with all-missing entries is uniform over fluid-types. We used this property to check our code.

6. Statistical inference with the Cut-Model. As noted in Section 3, the training and test data are gathered under different conditions (“laboratory” and “casework-like”). This motivates a second inference framework called Cut-Model inference (Liu, Bayarri and Berger, 2009; Plummer, 2015). The Cut-Model inference was developed as a robust variant of Bayesian inference. Carmona and Nicholls (2020) show that it is a coherent belief update in the sense of Bissiri, Holmes and Walker (2016). Cut-Models, which resemble Transfer Learning and the Power Prior (see Carvalho and Ibrahim (2021) and references therein), are relevant when we have two data sets with shared parameters and similar but possibly distinct observation models. The straightforward Bayesian approach would be model elaboration. However, since we have a clear overall loss (predictive performance on the test data), a strategy that varies and selects the inference procedure (Jacob et al., 2017) may be a principled alternative. In a Cut-Model setting, we regard the model that we developed for the labeled training data as potentially misspecified for the unlabeled test data, and we stop the test data from informing the parameters of the labeled data.

As Plummer (2015) points out, Cut-Model inference is a kind of Bayesian Multiple Imputation with two stages. In the “imputation stage”, we sample the posterior for the subtype-clustering $Q|\mathbf{X}_{\mathcal{T}}$, $Q \in \Xi_{\mathcal{T}}^*$ of labeled profiles using only labeled data $(y_i, x_i)_{i \in \mathcal{T}}$. In the “analysis stage”, we sample $R|\mathbf{X}, Q$, the posterior for all profile-subtypes conditioned on the subtype assignment Q of the labeled data. This two-stage setup stops the unlabeled profiles from informing the subtype-grouping of the labeled profiles. When unlabeled profiles come from a sample population, which differs from the sample population of labeled profiles, this may improve calibration.

Besides being robust, coherent, and principled, Cut-Model inference has a fourth appealing feature called “interoperability” by Nicholson et al. (2022). This means that the inference breaks up into stages, which respect the modular labeled/unlabeled structure of the data and makes it easy for different teams of researchers to work separately on different parts of the overall inference. In the imputation stage, subtype partitions Q for the labeled data can be sampled in advance. This step is moderately time-consuming but only has to be done once and not repeated for every new collection of unlabeled profiles x_i , $i \in \mathcal{U}$ as is necessary in Bayesian inference targeting $R|\mathbf{X}$. In the analysis stage, MCMC simulation of $R|\mathbf{X}, Q$ is fast, converges rapidly, and parallelizes well over different realizations of Q passed through from the imputation stage. This makes it safer in the hands of an inexperienced MCMC user.

When choosing between Bayesian and Cut-Model inference, we favor the inference framework that gives the best-calibrated posterior probabilities for true fluid-types in held-out data: in our case, the test data set. We explored Cut-Model inference because we expected problems arising from the model conflict between training and test data, especially when the number of unlabeled profiles U was of the same order as the number T of labeled profiles. However, we will see in Section 8 that the two inference schemes give essentially identical results, even when \mathcal{U} has many elements. This reflects the fact that there is no real evidence for misspecification. However, the “operational” advantages remain, and so we recommend Cut-Model inference for this type of analysis.

6.1. *The Cut-Model Posterior.* Let $Q = (Q_1, \dots, Q_F)$ give the partitions of the labeled data in each fluid-type (a “joint partition” with $Q_f \in \Xi_{\mathcal{T}_f}^{J_f}$ and $Q \in \Xi_{\mathcal{T}}^*$). We define

$$\Xi_{\mathcal{T}_f \cup \mathcal{V}_f}^{J_f}(Q_f) = \{P \in \Xi_{\mathcal{T}_f \cup \mathcal{V}_f}^{J_f} : P_k \cap \mathcal{T}_f = Q_{f(k)}, k = 1, \dots, K_f\}$$

to be the set of partitions of the labeled and unlabeled data that are consistent with a given partition Q_f of the labeled data in fluid-type f , and let

$$(17) \quad \Xi_{\mathcal{T}, \mathcal{V}}^*(Q) = \Xi_{\mathcal{T}_1 \cup \mathcal{V}_1}^{J_1}(Q_1) \times \Xi_{\mathcal{T}_2 \cup \mathcal{V}_2}^{J_2}(Q_2) \times \dots \times \Xi_{\mathcal{T}_F \cup \mathcal{V}_F}^{J_F}(Q_F)$$

be the set of joint partitions consistent with Q for fixed assignment partition \mathcal{V} . Finally,

$$\Xi_{\mathcal{T}, \mathcal{U}}^*(Q) = \bigcup_{\mathcal{V} \in \Psi_{\mathcal{U}}} \Xi_{\mathcal{T}, \mathcal{V}}^*(Q)$$

denotes the set of all joint partitions of the samples in the full dataset that contain Q as a joint sub-partition. If $R \in \Xi_{\mathcal{T}, \mathcal{U}}^*(Q)$, then $\{R\}$ and $\{Q, R, \mathcal{V}\}$ are the same events since $Q = Q(R)$ via $Q_{f(k)} = R_{f(k)} \cap \mathcal{T}_f$ for $f \in \mathcal{F}$ and $k = \{1, \dots, K_f\}$ and $\mathcal{V} = \mathcal{V}(R)$ via $\mathcal{V}_f = \bigcup_{k=1}^{K_f} R_{f(k)} \cap \mathcal{U}$.

The Cut-Model posterior for $R \in \Xi_{\mathcal{T}, \mathcal{U}}^*$ and $Q = Q(R)$ is then

$$(18) \quad \begin{aligned} \pi_{\text{cut}}(R|\mathbf{X}) &= \pi_{\text{cut}}(R, Q|\mathbf{X}) \\ &\equiv \pi(R|\mathbf{X}, Q) \pi(Q|\mathbf{X}_{\mathcal{T}}), \end{aligned}$$

with $Q \in \Xi_{\mathcal{T}}^*$ and $R \in \Xi_{\mathcal{T}, \mathcal{U}}^*(Q)$. The factors involved are

$$\pi(R|\mathbf{X}, Q) = \pi_R(R|Q) \frac{p(\mathbf{X}|R)}{p(\mathbf{X}|Q)}$$

with $p(\mathbf{X}|Q)$ an intractable normalising constant and

$$\pi(Q|\mathbf{X}_{\mathcal{T}}) \propto \pi(Q) p(\mathbf{X}_{\mathcal{T}}|Q).$$

Cut-Model inference is not Bayesian inference. The relation between the Cut posterior in Equation 18 and the Bayes posterior $\pi(R|\mathbf{X}) \propto \pi_R(R) p(\mathbf{X}|R)$ in Equation 16 is

$$\begin{aligned} \pi_{\text{cut}}(R|\mathbf{X}) &\propto \pi(R|\mathbf{X}) p(\mathbf{X}_{\mathcal{T}}|Q) / p(\mathbf{X}|Q) \\ &= \pi(R|\mathbf{X}) / p(\mathbf{X}_{\mathcal{U}}|\mathbf{X}_{\mathcal{T}}, Q), \end{aligned}$$

where $\mathbf{X} = (X_{\mathcal{T}}, X_{\mathcal{U}})$ is used to obtain the second line. We get the Cut-posterior by weighting the Bayes posterior with the (inverse of the) predictive probability for the new data $\mathbf{X}_{\mathcal{U}}$, leading to completely removing the influence of the new data on Q . The factor $p(\mathbf{X}_{\mathcal{T}}|Q)$ in the numerator is readily evaluated using Equation 13 (with $R \rightarrow Q$ and $\mathbf{X} \rightarrow \mathbf{X}_{\mathcal{T}}$). However, as

$$p(\mathbf{X}|Q) = \sum_{R \in \Xi_{\mathcal{T}, \mathcal{U}}^*(Q)} p(\mathbf{X}|R) \pi_R(R|Q)$$

is an intractable function of the parameter Q , we cannot target $\pi_{\text{cut}}(R|\mathbf{X})$ easily with MCMC.

In order to treat the intractable parameter-dependent constant $p(\mathbf{X}|Q)$, we sample the Cut-posterior in Equation 18 using nested MCMC (Plummer, 2015): we run MCMC targeting $\pi(Q|\mathbf{X}_{\mathcal{T}})$ giving samples $\{Q^{(t)}\}_{t=1}^{T_0}$ of partitions of the labeled data and then, for each $t \in \{1, \dots, T_0\}$, simulate a “side-chain” $\{R^{(t, t')}\}_{t'=1}^{T_1}$ targeting $\pi(R|\mathbf{X}, Q^{(t)})$. In the side-chain, the labeled profiles in $Q^{(t)}$ have fixed row-partitions, while the fluid-types and subtypes of

the unlabeled profiles (in R but not in $Q^{(t)}$) are updated. The intractable factor $p(\mathbf{X}|Q^{(t)})$ cancels in the Metropolis-Hastings acceptance probability in this second MCMC. We run the side-chain to equilibrium and take the final state as our sample by setting $R^{(t)} = R^{(t, T_1)}$ for all $t \in \{1, \dots, T_0\}$. The set of samples $\{R^{(t)}\}_{t=1}^{T_0}$ is, asymptotically in T_0 and T_1 , distributed according to $\pi_{\text{cut}}(R|\mathbf{X})$. The downside of nested MCMC is that we have to accept "double asymptotics" for convergence to target. However, the set $\{Q^{(t)}\}_{t=1}^{T_0}$ can be recycled for many different sets of unlabeled profiles, and the side chains targeting $\pi(R|\mathbf{X}, Q^{(t)})$ parallelize perfectly and converge very rapidly.

We can take the Cut-Model approach further. In Equation 18, we cut the feedback from unlabeled profiles into the row-clustering of labeled profiles, but the unlabeled profiles still interact with one another in $\pi(R|\mathbf{X}, Q)$. We can cut these interactions by simply taking the unlabeled profiles $i \in \mathcal{U}$ one at a time in separate Cut-posteriors, proceeding as above with $\mathcal{U} = \{i\}$. Such a setup enables the side-chains to be constructed by using a Gibbs sampler that reaches equilibrium in a single step.

7. Markov Chain Monte Carlo methods. We used Metropolis-Hastings Markov chain Monte Carlo (MCMC) to target $\pi(R|\mathbf{X})$ and $\pi_{\text{cut}}(R|\mathbf{X})$. The MCMC is constructed by specifying our own proposals, each of which operates on one profile at a time to update R . The proposal operation on a labeled profile is restricted to its fluid-type but updates its subtype assignment within the given fluid-type (see Appendix F.1). Additional proposals are implemented to update \mathcal{V} (see Appendices F.2 and F.3), and in conjunction with the subtype proposal operation above, they update the classification of unlabeled profiles in R . Of the updates on \mathcal{V} , the Gibbs sampler (in Appendix F.3) selects a new subtype across all subtypes of all fluid-types. As this update is rather expensive to compute, we have only used it in the Nested MCMC targeting the Cut-Model for the "side-chains" described at the end of Section 6.1.

All details of our MCMC, including proposals and acceptance probabilities, are given in Appendix F with a summary of typical runtimes, effective sample sizes (ESS), and implementation checks in Appendix F.4.

8. Method Testing.

8.1. Datasets. In order to evaluate our method, we use two mRNA profile datasets, a training set and a test set, consisting of 321 and 46 profiles, respectively. The true body fluid-type of each profile is known in both datasets. The number of profiles in each dataset and the markers used for classification are summarised in Table 1. Two "housekeeping-markers" are also reported. They are used to give an indication of the quality of the sample and as a positive control for the laboratory process. Details of sample collection and data generation can be found in Appendix B.

8.2. Testing procedure. LOOCV on the training data was used to evaluate the goodness-of-fit and classification performance of the trained model. These tests essentially confirmed our prior hyperparameter choices before moving on to the test data. For each fold of LOOCV, the label of one profile $y_i \in \mathcal{T}$ in the training data is treated as unknown, and then Bayes and Cut-Model inference is applied to estimate $\Pr(y_i = f|\mathbf{X}_{\mathcal{T}-i}, x_i)$, so $\mathcal{U} = \{i\}$, $U = 1$ and $\mathcal{T} = \mathcal{T} \setminus \{i\}$.

The training data were used to develop our biclustering prior, and in the canonical experiments in Section 8.4 and Section 8.5, we check the accuracy of predicted fluid-types and evaluate how well calibrated our posterior for fluid-type assignments are. We treat the training data as labeled data and the test data as unlabeled data. The test data were gathered under conditions designed to mimic casework, so these performance measures should give a better indication of future performance on casework data than would the training data.

We experimented with two kinds of classification schemes: “Single Profile Classification” (SPC) and “Joint Profile Classification” (JPC). SPC classifies each mRNA profile in a separate analysis, with $U = 1$, leading to mutually independent posterior fluid-type distributions of unlabeled mRNA profiles. The LOOCV analyses are all SPC analyses, and we carry out a further 46 Bayes and Cut-Model SPC analyses on the test data. JPC allows joint classification with $U > 1$ in each analysis. For the test dataset, we obtain the classifications of all $U = 46$ mRNA profiles in a single JPC analysis using Bayesian inference and again in the Cut-Model.

We set $J_f = 5$ and $L_g = M_g$ for the MDP bounds on the number of row and column partitions for all $f, g \in \mathcal{F}$ in all analyses except those in Section I, where we check the goodness of fit for these choices. Prior hyper-parameters $a_{f,g}$ and $b_{f,g}$ are given (Appendix E) and fixed across all analyses.

Our experiments are listed in Table 8 in Appendix F.4 with a brief statement of the purpose of the analysis and ESS values for the associated MCMC.

8.3. Leave-one-out cross validation. In this section, we use LOOCV on the training data to check our model assumptions by estimating posterior probabilities for the true fluid-types of held-out profiles. The training data is a relatively large data set, and the test data do not include any MTB profiles. Hence, although we expect to overfit the training data, the LOOCV/SPC setup enables us to gain some insight into the performance before moving on to the test data.

8.3.1. Classifying using the Maximum a Posteriori type. Figure 3 summarises results for Bayesian inference on the training data. Figure 8 in Appendix H gives the corresponding results for the Cut-Model, which are very similar to those in Figure 3. The posterior probability for the correct type is close to one for most mRNA profiles. In both figures, panels (a)–(e) display the distributions of the posterior probabilities for the correct types of unlabeled mRNA profiles (i.e., each held-out training profile), while panel (f) presents the confusion table obtained from labeling profiles with the posterior mode of the fluid type. This does slightly better than naïve assignment of types using a majority target-marker rule (Table 5), as it handles ambiguous (tied) cases more reliably.

Some CVF and MTB profiles have low posterior probabilities (< 0.5) for the correct type. For those profiles, if they are from CVF samples, their posterior mode types are MTB, and vice versa. For profiles from SLV, BLD and SMN samples, all of them have posterior modes equal to their respective true types. This is also reflected in their high posterior probabilities for the correct type, which are all > 0.5 , with most of them ≈ 1 .

The similarity between Bayesian and Cut-Model inference is expected in a LOOCV/SPC analysis of the training data. A single profile feeds very little information into the fluid sub-type partition, so the sub-type partitions of \mathcal{T}_{-i} are much the same whether held-out profile i is present (Bayes) or absent (Cut).

8.3.2. Likelihood ratios for classification of training data. Given the focus on Likelihood ratios in the courtroom, we calculate Bayes factors (BFs), measuring the strength of the evidence for the correct type over the aggregate group of the other four fluid-types. We do this separately for each profile in the training data (i.e., for each fold of the LOOCV) presenting results obtained using Cut-Model inference (Table 2, Bayesian analysis gives essentially the same results). Using the BF scale given by Jeffreys (1998), we find “decisive evidence” ($\log_{10} \text{BF} > 2$) for the correct body fluid-type for most folds of the LOOCV. Two of the 321 profiles provided “strong evidence” *against* their correct type ($-1.5 < \log_{10} \text{BF} < -1$) and one was “very strongly” against ($-2 < \log_{10} \text{BF} < -1.5$). These were CVF and MTB profiles.

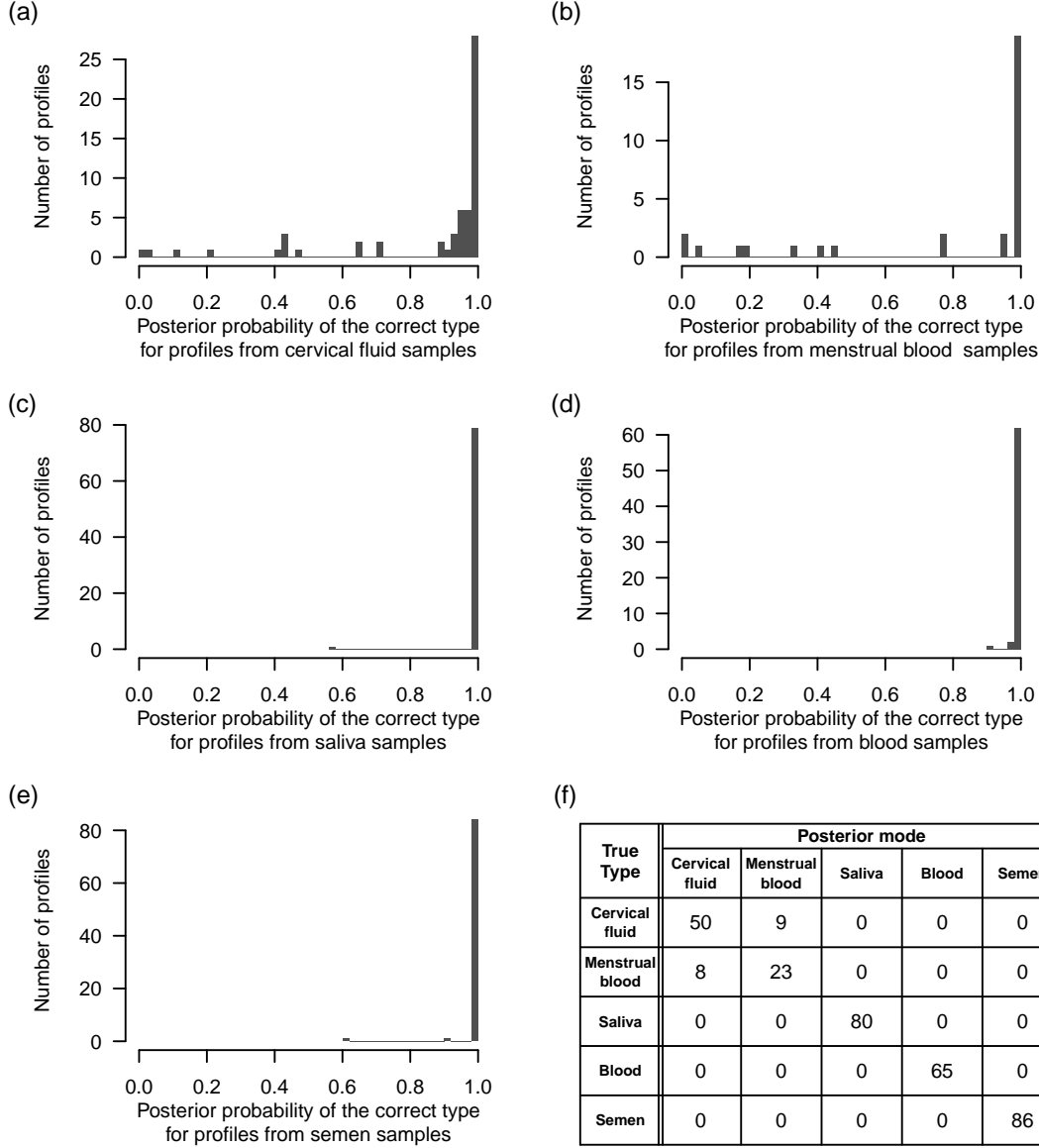


FIG 3. Posterior mode probability and mode of the correct type (for RNA profiles in the training set) estimated from the LOOCV analysis with the full Bayes approach.

8.4. *Fluid classification of an independent test set.* In this section, we compare results from four experiments, pairing each of Bayesian and Cut-Model inference with SPC and JPC analyses. The likelihood ratios reported here give some indication of the level of confidence that the method will provide in evidence for casework data.

8.4.1. *Comparison across analyses.* A high level of similarity is observed in the posterior probabilities for the correct types of mRNA profiles in the test dataset across all four analysis designs as shown in Figure 4, which plots Cut-Model posterior probabilities against Bayes for SPC and JPC. If the trained model, that we developed by applying BDP to the training data, does not fit the test data well, then we would expect this to show up in different posterior probabilities in the Bayes and Cut-Model JPC analyses. If the test data has multiple profiles from sub-types that are not well represented in the training data, then the joint

TABLE 2

Bayes factors (log base 10) measuring the strength of the evidence for the correct type estimated from the LOOCV on the training set in Cut-Model inference.

True Type	\log_{10} Bayes factor (LR)						
	$[-2, -1]$	$[-1, -0.5]$	$[-0.5, 0]$	$(0, 0.5]$	$(0.5, 1]$	$(1, 2]$	$(2, \infty)$
CVF	1	1	1	3	7	12	34
MTB	2	1	2	3	1	3	19
SLV	0	0	0	0	1	0	79
BLD	0	0	0	0	0	1	64
SMN	0	0	0	0	1	1	84

fluid sub-type partition Q of the training data \mathcal{T} may be different depending on whether it is formed jointly (Bayes) or independently (Cut) of the test data \mathcal{U} . The comparison is made in panel (b) of Figure 4. Bayesian inference assigns somewhat higher posterior probabilities to the true fluid-type for the unlabeled test data, though the effect is weak (for example, the modal fluid-type for any given profile is equal in the two analyses).

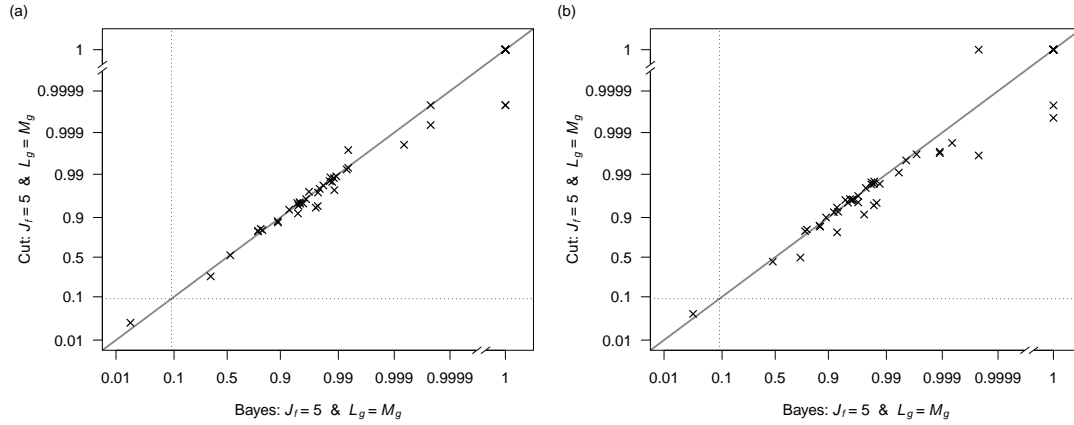


FIG 4. Comparison of the posterior probability of the correct types (for mRNA profiles in the test set) between Bayesian- and Cut-Model inference. Panel (a) presents results obtained from analyzing each test mRNA profile one at a time, while panel (b) shows that from analyzing all 46 test mRNA profiles jointly.

Confusion tables for the classification of the test data using the posterior mode of fluid-type in SPC and JPC analyses (identical for Bayes- and Cut-Model inference) are given in Table 9 in Appendix H. Two profiles are miss-classified, and the SPC and JPC classifications differ by reassignment of two profiles of 46.

8.4.2. *Likelihood ratios for classification of test data.* Table 3 presents Bayes factors (log base 10) measuring evidence for correct type assignment for each mRNA profile in the test set using SPC in Cut-Model inference. Very similar results (not presented) are obtained for the other three combinations of inference framework (Bayes/Cut) and classification schemes (SPC/JPC). For the majority of the mRNA profiles, there is at least strong evidence ($\log_{10} \text{BF} > 1$) for the correct body fluid-type over the rest of the four fluid-types. Of the 46 profiles in the test set, one profile provides “moderate evidence” against its true type, a CVF profile favoring MTB.

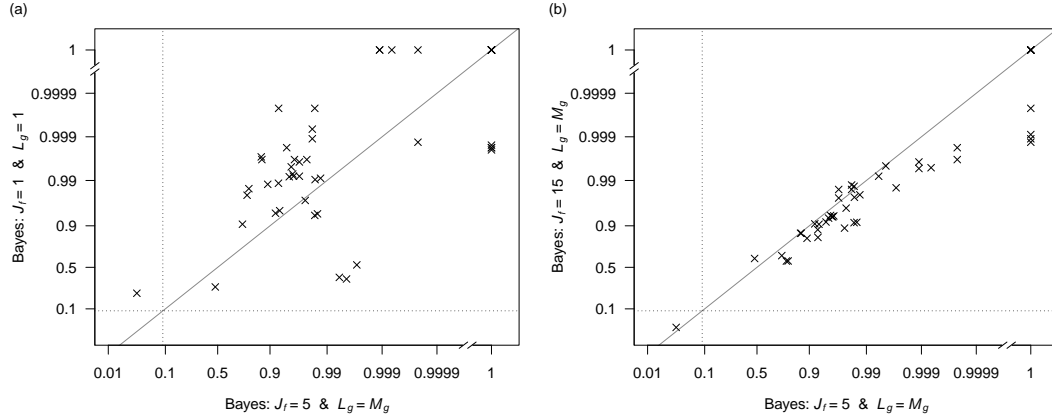
8.4.3. *Experiments varying the upper bound on partition number.* We set $J_f = 5$ and $L_g = M_g$ for all $f, g \in \mathcal{F}$ in all analyses above (the default BDP setup for our data). In order

TABLE 3

Bayes factors (log base 10) measuring the strength of evidence for the correct type estimated using SPC on the test set in Cut-Model inference.

True Type	\log_{10} Bayes factor (LR)						
	$[-2, -1]$	$[-1, -0.5]$	$[-0.5, 0]$	$(0, 0.5]$	$(0.5, 1]$	$(1, 2]$	$(2, \infty)$
CVF	0	1	0	0	1	13	9
SLV	0	0	0	0	0	0	10
BLD	0	0	0	0	0	0	2
SMN	0	0	0	1	0	3	6

FIG 5. Comparing the posterior probabilities of the correct types estimated by Bayesian inference for the 46 mRNA profiles (a) between the default model ($J_f = 5, L_g = M_g$) and ($J_f = 1, L_g = 1$), and (b) between the default model and ($J_f = 15, L_g = M_g$) $\forall f, g \in \mathcal{F}$. For legibility, the positions on axes are in logit-space, while the labels represent the corresponding probability values.



to investigate whether the choice of J_f has an impact on our results, we performed a sensitivity analysis with JPC on the test data with the following (J_f, L_g) combinations: $(1, 1)$, $(1, M_g)$, $(10, M_g)$ and $(15, M_g)$ for all $f, g \in \mathcal{F}$. Results are given in Figure 5 and in Figure 9 in Appendix I. It is clear from the training data (Figure 1) that sub-types are a feature of the sample population for mRNA profiles. Figure 5 suggests that, when there is no biclustering, i.e., $(J_f = 1, L_g = 1) \forall f, g \in \mathcal{F}$, the posterior probabilities of the correct type are more dispersed than the default model. Specifically, when the posterior probability of the correct type is approximately 0.99, the corresponding probability estimated without biclustering can range between 0.5 and 0.9999. Removing all biclustering tends to give posterior probabilities for correct types that are slightly higher than what we get with biclustering, as we might expect in a model with fewer parameters. In contrast, when $(J_f, L_g) = (10, M_g) \forall f, g \in \mathcal{F}$ or $(J_f, L_g) = (15, M_g) \forall f, g \in \mathcal{F}$, the posterior probabilities of the correct type are in fair agreement with the default model. There is no evidence for interaction between the choice of Bayesian or Cut-Model inference and the (J_f, L_g) -settings (Figure 9, Appendix I).

The posterior distribution of the number of subtypes within each fluid-type shifts to slightly larger numbers of subtypes, when J_f is increased from 5 to 10 for all $f \in \mathcal{F}$ (Figure 10, Appendix I). Similarly, there is little change when increasing J_f from 10 to 15 for all $f \in \mathcal{F}$. Considering the distributions of the numbers of subtypes when $J_f = 15$, the posterior probability for six or more subtypes is small (less than 0.1) except for SMN, where it is around 0.4. The SMN samples may require more than five subtypes to characterize the within-type heterogeneity in the marker profiles. This suggests there may be some value in taking a Poisson-Dirichlet-Process and estimating upper bounds separately for each fluid-

type. However, SMN profiles are rather easy to classify, so this is unlikely to make much difference to the assigned class labels themselves.

8.5. Calibration. In a forensic setting, we need well-calibrated posterior probabilities for the assignment of fluid-types to unlabeled profiles in order to ensure that they give a meaningful measure of the uncertainty in fluid-type classification (Dawid, 1982; Meuwly, Ramos and Haraksim, 2017; Morrison, 2021). We use a simple form of Beta-calibration (Kull, Filho and Flach 2017, Algorithm 1) as goodness-of-fit checks and show no evidence that greater complexity is needed. Beta-calibration can be seen as Platt-scaling (Platt, 2000) with a careful choice of regression covariates.

Suppose the true generative model for a binary profile $X \in \{0, 1\}^M$ with true fluid-type Y is $Y \sim p^*(\cdot)$ and $X \sim p^*(\cdot|Y)$. Let $\mathbf{X}_{\mathcal{T}}$ be the labeled data. When we observe $X = x$, we calculate posterior probabilities $\pi(y|\mathbf{X}_{\mathcal{T}}, x)$, $y \in \mathcal{F}$ using our model via MCMC. If these are well-calibrated, then

$$\pi = \Pr(Y = y|\pi(y|\mathbf{X}_{\mathcal{T}}, X) = \pi).$$

In analyses of the test data, we have observations (x_j, y_j) , $j \in \mathcal{T}$ with true fluid-type y_j and profiles x_i , $i \in \mathcal{U}$ with true fluid-type y_i , $i \in \mathcal{U}$ held out, so our estimated posterior $\hat{\pi}(y|\mathbf{X}_{\mathcal{T}}, x_i)$ is well calibrated if

$$(19) \quad \mathbb{I}_{y_i=y} \sim \text{Bernoulli}(\hat{\pi}(y|\mathbf{X}_{\mathcal{T}}, x_i)),$$

for any fixed $y \in \mathcal{F}$. We can test this using logistic regression.

A very naïve application of Platt scaling would regress $\mathbb{I}_{y_i=y}$ on the covariate $\hat{\pi}_i = \hat{\pi}(y|\mathbf{X}_{\mathcal{T}}, x_i)$ with logistic link $\text{logit}(p_i) = \eta_i$ and $\eta_i = \alpha + \beta \hat{\pi}_i$. However, we cannot represent the identity map from $\hat{\pi}_i$ to p_i in this parameterization, so the recalibrated probabilities could never match posterior probabilities. However, if $\hat{\pi}_i$ is replaced with

$$z_i = \text{logit}(\hat{\pi}_i)$$

as our covariates, and we fit the logistic regression model

$$\mathbb{I}_{y_i=y} \sim \text{Bernoulli}(p(\eta_i))$$

with linear predictor $\eta_i = \alpha + \beta z_i$, then the success probability in the regression is

$$(20) \quad p(\alpha + \beta \text{logit}(\hat{\pi}_i)) = \frac{\hat{\pi}_i^\beta}{e^{-\alpha}(1 - \hat{\pi}_i)^\beta + \hat{\pi}_i^\beta}.$$

This is the simplest of the Beta-calibration maps considered in Kull, Filho and Flach (2017). If $\alpha = 0$ and $\beta = 1$ then $p(\eta_i) = \hat{\pi}_i$, so regressing $\mathbb{I}_{y_i=y}$ on z_i should produce $\hat{\alpha} \simeq 0$ and $\hat{\beta} \simeq 1$ if $\hat{\pi}$ is well calibrated. The recalibration map

$$\mu(\pi) = p(\alpha + \beta \text{logit}(\pi))$$

is then the identity map. Any departure from the identity can be interpreted as an adjustment to the posterior probabilities required in order to give an improved calibration and make $\mu(\pi)$ better match $p^*(y|x)$.

We will test calibration using the posterior probabilities for the classification of profiles in the test data. Recall the setup: the test data are added to the training data; the training data \mathcal{T} are labeled, and the test data \mathcal{U} are unlabeled. The classification can be executed by Bayesian inference or Cut-model inference, and prediction of the missing labels can be performed either one profile at a time or simultaneously as a group. Treating the transformed posterior probabilities as covariates in this regression, the BLD, SLV and SMN data are linearly separable, so we cannot learn “better values”. Also, there are no MTB sample profiles in the test

data. However, there are MTB sample profiles in the training data, and the MTB and CVF profiles sometimes share similar patterns, so these allow us to test calibration. We re-label profiles as “CVF” and “non-CVF” and check the calibration of the posterior probabilities for the assignment of a test profile to CVF.

We construct a logistic regression with true fluid-types $y_i = 1$ (CVF) or $y_i = 0$ (non-CVF) and fix $y = 1$ in Equation 19. This analysis examines whether our posterior probabilities for CVF in the test data are well-calibrated. If the answer is yes, then this supports our full prior and likelihood model and supports our claim that BLD, MTB, SLV and SMN posterior probabilities are likewise.

In the following, we have a small number of values where $\hat{\pi}_i = 0$ or 1. In these cases, we know the exact posterior $\pi(1|\mathbf{X}_{\mathcal{T}}, x_i)$ is neither 0 nor 1, and the error is due to the rounding effect of Monte Carlo with finite sample size. When we transform from $\hat{\pi}$ to z , we take $z_i = f(\hat{\pi}(1|\mathbf{X}_{\mathcal{T}}, x_i))$ for $i \in \{k \in \mathcal{U} : y_k = 0 \text{ or } 1\}$ using a compressed logistic transformation, $f(\hat{\pi}) = \text{logit}((1 - 2d)\hat{\pi} + d)$ with $d = 0.0001$. We repeated the analysis with the logistic map but dropped the 0’s and 1’s, which produced essentially identical results.

Inference	$\hat{\alpha}(\text{s.e.})$	$\hat{\beta}(\text{s.e.})$	$p\text{-value}$
Single/Bayes	1.6(9)	0.9(3)	0.15
Joint/Bayes	2.0(1)	1.1(4)	0.11
Single/Cut	1.3(9)	0.9(3)	0.23
Joint/Cut	1.3(9)	1.0(4)	0.27

TABLE 4

Calibration results for the test data set: table entries give estimated recalibration parameter values fitted on posterior class probabilities estimated using two different inference frameworks (Bayes and Cut) and classifying the test data one profile by SPC or JPC. The p -value column gives the p -value for a deviance test with null corresponding to the hypothesis that the posterior probabilities are well-calibrated.

The fitted recalibration maps are shown in Table 4. We perform a simple deviance test for the null (well-calibrated) model with $(\alpha, \beta) = (0, 1)$ against $(\alpha, \beta) \in R^2$. There is no evidence for miss-calibration in any of the analyses ($p \geq 0.05$), and the slope estimates are all close to one. A value of $\alpha > 0$ would indicate that the recalibrated posterior probability is bigger than the uncalibrated posterior probability, uniformly over the latter. However, this is not significant. There is perhaps a weak case for better calibrated Cut-model inference, as there is less evidence against the null model for the Cut-model analyses.

9. Concluding remarks. Well-calibrated probabilistic statements on body fluid classification are important in a forensic setting. We have addressed this problem using statistical modeling, developing a biclustering model that provides a flexible and transparent approach to characterize the patterns in the mRNA profiles for body fluid classification and quantifies uncertainty in the assignment of class labels. The model has a three-level nested hierarchical structure consisting of the fluid-type, subtype and marker levels. The assignment of unlabeled profiles to fluid-types is random, so subtypes partition a ground set, which is random. The BDP differs from related nested biclustering methods (Lee et al., 2013; Guha and Baladayuthapani, 2016; Li et al., 2020), which have two levels of hierarchy and partition a fixed ground set.

Work by Tian et al. (2020); Wohlfahrt et al. (2023); Ypma et al. (2021), employing machine learning methods, e.g., random forest, SVM, neural networks etc., also model heterogeneity in mRNA profiles within a fluid-type. They have the advantage of flexibility. Our statistical modeling approach makes interpreting patterns of heterogeneity within fluid-types more straightforward. This will help users assess the suitability of our methods in the context

of the problem at hand and communicate results. Although in some respects simpler than the models given above, our model is well-specified, as evidenced by well-calibrated measures of confidence in class labels.

One very helpful feature of our approach is that we can integrate out all random variables below the level of fluid subtypes. The parameter space we actually sample is substantially reduced, facilitating MCMC simulation and making it easier for practitioners to use the tool.

We are fortunate to have a training dataset with 321 labeled mRNA profiles that is representative of the population, as evidenced by the fact that the model is well calibrated for test data, regardless of the inference framework (Bayes/Cut-Model) or classification scheme (JPC/SPC). Sensitivity analysis showed that results are robust to the choice of the maximum number of subtypes when we increase J_f from five.

We now make some recommendations on the choice of Bayes or Cut posteriors and the choice of joint or separate analyses. Data analysis in a forensic setting is constrained by legal and ethical considerations, so the choice is rather clear: we would always perform a separate analysis for each profile in \mathcal{U} , and Cut-Model inference would likely be favored, as it does not allow the casework sample to influence our beliefs about structure in the labeled training data.

In applications outside the forensic setting, there will be a loss function, possibly unstated, and typically some measure of posterior concentration on the unknown true fluid-types. The question then is whether we wish to minimize the total risk across all profiles jointly or minimize it separately for each unlabeled profile. For example, if there are two profiles and we ask “are these the same class?” then the joint analysis is more straightforward, and the interaction of the unlabeled profiles informs their joint class. A similar issue arises in shrinkage analysis of data from multiple sources. Bayesian inference integrates all the data, so will generally give lower variance. However, it is expected to be more biased when the sample populations for labeled and unlabeled data differ. In all settings, Cut-model inference has the operational advantages listed in Section 6.1.

In the analyses presented so far, we do not explicitly handle the scenario where profiles show patterns distinctive from those exhibited by candidate fluid-types, possibly because they are from a non-target material $f' \notin \mathcal{F}$ or a sample of mixed types. However, such anomalies are easily identified from the output subtype partitions produced by our method. Profiles with patterns that differ substantially from profiles in the training data tend to enter any given fluid-type as a singleton subtype. A profile with an unusually high posterior probability of being a singleton therefore warrants careful inspection to check its data quality and whether it might be none of the candidate fluid-types or has mixed fluid-types.

In future work, we plan to extend our model to treat mixtures and non-fluid samples. The current method already permits including an extra fluid-type to explicitly accommodate a profile that fits none of the candidate fluid-types. A parametric model for mixed fluid types also seems to be within reach of careful statistical modeling and computation of the kind we have given, though presents more of a challenge. In summary, we present a novel biclustering method that provides meaningful uncertainty statements and interpretable results on the classification of body fluids in a forensic setting, and this provides the foundation for more complex scenarios likely to be encountered in casework.

<https://github.com/gknicholls/Forensic-Fluids> gives code and data.

REFERENCES

- AKUTSU, T., YOKOTA, I., WATANABE, K. and SAKURADA, K. (2020). Development of a multiplex RT-PCR assay and statistical evaluation of its use in forensic identification of vaginal fluid. *Legal Medicine* **45** 101715. <https://doi.org/10.1016/j.legalmed.2020.101715>

- AKUTSU, T., YOKOTA, I., WATANABE, K., TOYOMANE, K., YAMAGISHI, T. and SAKURADA, K. (2022). Precise and comprehensive determination of multiple body fluids by applying statistical cutoff values to a multiplex reverse transcription-PCR and capillary electrophoresis procedure for forensic purposes. *Legal Medicine* **58** 102087.
- BISSIRI, P. G., HOLMES, C. C. and WALKER, S. G. (2016). A general framework for updating belief distributions. *Journal of the Royal Statistical Society: Series B (Statistical Methodology)* **78** 1103–1130. <https://doi.org/10.1111/rssb.12158>
- CARMONA, C. U. and NICHOLLS, G. K. (2020). Semi-Modular Inference: enhanced learning in multi-modular models by tempering the influence of components. In *Proceedings of the 23rd International Conference on Artificial Intelligence and Statistics, AISTATS 2020* (C. SILVIA and R. CALANDRA, eds.) 4226–4235. PMLR arXiv: 2003.06804. <https://doi.org/10.48550/arXiv.2003.06804>
- CARVALHO, L. M. and IBRAHIM, J. G. (2021). On the normalized power prior. *Statistics in Medicine* **40** 5251–5275. <https://doi.org/10.1002/sim.9124>
- DAWID, A. P. (1982). The well-calibrated Bayesian. *Journal of the American Statistical Association* **77** 605–610.
- DE ZOETE, J., CURRAN, J. and SJERPS, M. (2016). A probabilistic approach for the interpretation of RNA profiles as cell type evidence. *Forensic Science International: Genetics* **20** 30–44.
- FERGUSON, T. S. (1973). A Bayesian Analysis of Some Nonparametric Problems. *The Annals of Statistics* **1** 209–230. Publisher: Institute of Mathematical Statistics.
- FUJIMOTO, S., MANABE, S., MORIMOTO, C., OZEKI, M., HAMANO, Y., HIRAI, E., KOTANI, H. and TAMAKI, K. (2019). Distinct spectrum of microRNA expression in forensically relevant body fluids and probabilistic discriminant approach. *Scientific Reports* **9** 14332. Number: 1 Publisher: Nature Publishing Group. <https://doi.org/10.1038/s41598-019-50796-8>
- GHOSAL, S. and VAN DER VAART, A. (2017). *Fundamentals of Nonparametric Bayesian Inference*. Cambridge Series in Statistical and Probabilistic Mathematics. Cambridge University Press.
- GUHA, S. and BALADANDAYUTHAPANI, V. (2016). A nonparametric Bayesian technique for high-dimensional regression. *Electronic Journal of Statistics* **10** 3374 – 3424. <https://doi.org/10.1214/16-EJS1184>
- HARBISON, S. and FLEMING, R. (2016). Forensic body fluid identification: state of the art. *Research and Reports in Forensic Medical Science* **6** 11–23. Publisher: Dove Medical Press _eprint: <https://www.tandfonline.com/doi/pdf/10.2147/RRFMS.S57994>. <https://doi.org/10.2147/RRFMS.S57994>
- HE, H., HAN, N., JI, C., ZHAO, Y., HU, S., KONG, Q., YE, J., JI, A. and SUN, Q. (2020). Identification of five types of forensic body fluids based on stepwise discriminant analysis. *Forensic Science International: Genetics* **48** 102337. <https://doi.org/10.1016/j.fsigen.2020.102337>
- HOCHREITER, S., BODENHOFER, U., HEUSEL, M., MAYR, A., MITTERECKER, A., KASIM, A., KHAMIAKOVA, T., VAN SANDEN, S., LIN, D., TALLOEN, W., BIJNENS, L., GÖHLMANN, H. W. H., SHKEDY, Z. and CLEVERT, D.-A. (2010). FABIA: factor analysis for bicluster acquisition. *Bioinformatics* **26** 1520–1527. <https://doi.org/10.1093/bioinformatics/btq227>
- HYVÄRINEN, A. (1999). Survey on independent component analysis. *Neural computing surveys* **2** 94–128.
- IACOB, D., FÜRST, A. and HADRY, T. (2019). A machine learning model to predict the origin of forensically relevant body fluids. *Forensic Science International: Genetics Supplement Series* **7** 392–394.
- JACOB, P. E., MURRAY, L. M., HOLMES, C. C. and ROBERT, C. P. (2017). Better together? Statistical learning in models made of modules. arXiv: 1708.08719 Pages: 1-31.
- JEFFREYS, H. (1998). *The theory of probability*. OuP Oxford.
- JHA, C. (2018). A Nonparametric Bayesian Method for Clustering of High-Dimensional Mixed Dataset. arXiv:1808.04045 [stat]. <https://doi.org/10.48550/arXiv.1808.04045>
- KULL, M., FILHO, T. S. and FLACH, P. (2017). Beta calibration: a well-founded and easily implemented improvement on logistic calibration for binary classifiers. In *Proceedings of the 20th International Conference on Artificial Intelligence and Statistics* (A. SINGH and J. ZHU, eds.). *Proceedings of Machine Learning Research* **54** 623–631. PMLR.
- LEE, J., MÜLLER, P., ZHU, Y. and JI, Y. (2013). A Nonparametric Bayesian Model for Local Clustering With Application to Proteomics. *Journal of the American Statistical Association* **108** 775–788. <https://doi.org/10.1080/01621459.2013.784705>
- LEGG, K. M., POWELL, R., REISDORPH, N., REISDORPH, R. and DANIELSON, P. B. (2014). Discovery of highly specific protein markers for the identification of biological stains. *ELECTROPHORESIS* **35** 3069–3078. _eprint: <https://onlinelibrary.wiley.com/doi/pdf/10.1002/elps.201400125>. <https://doi.org/10.1002/elps.201400125>
- LI, Y., BANDYOPADHYAY, D., XIE, F. and XU, Y. (2020). BAREB: A Bayesian repulsive biclustering model for periodontal data. *Statistics in Medicine* **39** 2139–2151. _eprint: <https://onlinelibrary.wiley.com/doi/pdf/10.1002/sim.8536>. <https://doi.org/10.1002/sim.8536>

- LINDENBERGH, A., DE PAGTER, M., RAMDAYAL, G., VISSER, M., ZUBAKOV, D., KAYSER, M. and SIJEN, T. (2012). A multiplex (m) RNA-profiling system for the forensic identification of body fluids and contact traces. *Forensic Science International: Genetics* **6** 565–577.
- LIU, F., BAYARRI, M. J. and BERGER, J. O. (2009). Modularization in Bayesian analysis, with emphasis on analysis of computer models. *Bayesian Analysis* **4** 119–150. ISBN: 1936-0975. <https://doi.org/10.1214/09-BA404>
- MEEDS, E. and ROWEIS, S. (2007). Nonparametric Bayesian Biclustering Technical Report, Technical report, University of Toronto.
- MEUWLY, D., RAMOS, D. and HARAKSIM, R. (2017). A guideline for the validation of likelihood ratio methods used for forensic evidence evaluation. *Forensic science international* **276** 142–153.
- MORAN, G. E., ROČKOVÁ, V. and GEORGE, E. I. (2021). Spike-and-slab Lasso biclustering. *The Annals of Applied Statistics* **15** 148 – 173. <https://doi.org/10.1214/20-AOAS1385>
- MORRISON, G. S. (2021). In the context of forensic casework, are there meaningful metrics of the degree of calibration? *Forensic Science International: Synergy* **3** 100157. <https://doi.org/10.1016/j.fsisyn.2021.100157>
- MURUA, A. and QUINTANA, F. A. (2022). Biclustering via Semiparametric Bayesian Inference. *Bayesian Analysis* **17** 969 – 995. <https://doi.org/10.1214/21-BA1284>
- NICHOLSON, G., BLANGIARDO, M., BRIERS, M., DIGGLE, P. J., FJELDE, T. E., GE, H., GOUDIE, R. J. B., JERSAKOVA, R., KING, R. E., LEHMANN, B. C. L., MALLON, A.-M., PADELLINI, T., TEH, Y. W., HOLMES, C. and RICHARDSON, S. (2022). Interoperability of Statistical Models in Pandemic Preparedness: Principles and Reality. *Statistical Science* **37** 183–206. Publisher: Institute of Mathematical Statistics. <https://doi.org/10.1214/22-STS854>
- PERMAN, M., PITMAN, J. and YOR, M. (1992). Size-biased sampling of Poisson point processes and excursions. *Probability Theory and Related Fields* **92** 21–39. <https://doi.org/10.1007/BF01205234>
- PLATT, J. C. (2000). Probabilities for SV Machines. In *Advances in Large-Margin Classifiers* (A. J. Smola, P. Bartlett, B. Schölkopf and D. Schuurmans, eds.) 5, 61–73. The MIT Press, Cambridge, MA. <https://doi.org/10.7551/mitpress/1113.003.0008>
- PLUMMER, M. (2015). Cuts in Bayesian graphical models. *Statistics and Computing* **25** 37–43. <https://doi.org/10.1007/s11222-014-9503-z>
- REN, Y., SIVAGANESAN, S., ALTAYE, M., AMIN, R. S. and SZCZESNIAK, R. D. (2020). Biclustering of medical monitoring data using a nonparametric hierarchical Bayesian model. *Stat* **9** e279. <https://onlinelibrary.wiley.com/doi/pdf/10.1002/sta4.279> <https://doi.org/10.1002/sta4.279>
- RODRÍGUEZ, A., DUNSON, D. B. and GELFAND, A. E. (2012). The Nested Dirichlet Process. <https://doi.org/10.1198/016214508000000553> **103** 1131–1154. <https://doi.org/10.1198/016214508000000553>
- ROEDER, A. D. and HAAS, C. (2016). Body fluid identification using mRNA profiling. *Forensic DNA Typing Protocols* 13–31.
- ROČKOVÁ, V. and GEORGE, E. I. (2018). The spike-and-slab lasso. *Journal of the American Statistical Association* **113** 431–444.
- SIJEN, T. (2015). Molecular approaches for forensic cell type identification: on mRNA, miRNA, DNA methylation and microbial markers. *Forensic Science International: Genetics* **18** 21–32.
- TIAN, H., BAI, P., TAN, Y., LI, Z., PENG, D., XIAO, X., ZHAO, H., ZHOU, Y., LIANG, W. and ZHANG, L. (2020). A new method to detect methylation profiles for forensic body fluid identification combining ARMS-PCR technique and random forest model. *Forensic Science International: Genetics* **49** 102371. <https://doi.org/10.1016/j.fsigen.2020.102371>
- VEHTARI, A., GELMAN, A. and GABRY, J. (2017). Practical Bayesian model evaluation using leave-one-out cross-validation and WAIC. *Statistics and computing* **27** 1413–1432.
- WANG, W. and STEPHENS, M. (2021). Empirical Bayes matrix factorization. *The Journal of Machine Learning Research* **22** 120:5332–120:5371.
- WATANABE, S. (2012). A Widely Applicable Bayesian Information Criterion. *Journal of Machine Learning Research* **14** 867–897. arXiv: 1208.6338 ISBN: 1532-4435.
- WOHLFAHRT, D., TAN-TORRES, A. L., GREEN, R., BRIM, K., BRADLEY, N., BRAND, A., ABSHIER, E., NOGALES, F., BABCOCK, K., BROOKS, J. P. et al. (2023). A bacterial signature-based method for the identification of seven forensically relevant human body fluids. *Forensic Science International: Genetics* **65** 102865.
- XU, Y., LEE, J., YUAN, Y., MITRA, R., LIANG, S., MÜLLER, P. and JI, Y. (2013). Nonparametric Bayesian Bi-Clustering for Next Generation .g Count Data. *Bayesian analysis (Online)* **8** 759–780.
- YAN, H., WU, J., LI, Y. and LIU, J. S. (2022). Bayesian bi-clustering methods with applications in computational biology. *The Annals of Applied Statistics* **16** 2804 – 2831. <https://doi.org/10.1214/22-AOAS1622>
- YPMA, R. J. F., VAN WIJK, P. A. M., GILL, R., SJERPS, M. and VAN DEN BERGE, M. (2021). Calculating LR_s for presence of body fluids from mRNA assay data in mixtures. *Forensic Science International: Genetics* **52**. <https://doi.org/10.1016/J.FSIGEN.2020.102455>

- ZANINI, C. T. P. (2019). Dependent Mixtures and Random Partitions, Ph.D., The University of Texas at Austin, United States – Texas ISBN: 9798684602191.
- ZHANG, H., ZOU, Y., TERRY, W., KARMAUS, W. and ARSHAD, H. (2019). Joint Clustering With Correlated Variables. *The American Statistician* **73** 296–306. Publisher: Taylor & Francis _eprint: <https://doi.org/10.1080/00031305.2018.1424033>. <https://doi.org/10.1080/00031305.2018.1424033>
- ZUANETTI, D. A., MÜLLER, P., ZHU, Y., YANG, S. and JI, Y. (2018). Clustering distributions with the marginalized nested Dirichlet process. *Biometrics* **74** 584–594. _eprint: <https://onlinelibrary.wiley.com/doi/pdf/10.1111/biom.12778>. <https://doi.org/10.1111/biom.12778>

APPENDIX A: ESTIMATING FLUID-TYPE USING SIMPLE MAJORITY

In Table 5 we give a confusion table we get if we simply classify the fluid type of a profile in the training data by taking it to be the fluid type of the market group with the most amplified markers, so $\hat{y}_i = \arg \max_{g \in \mathcal{F}} \sum_{i \in \mathcal{M}_g} x_i$. For a row $f \in \mathcal{F}$ in the table, the table entry $N_{f,g}$ in column $g \in \mathcal{F}$ gives $N_{f,g} = \sum_{i \in \mathcal{T}_f} \mathbb{I}_{\hat{y}_i = g}$, so for example 17 MTB profiles in the training data were incorrectly classified by this naïve method as CVF.

TABLE 5

The posterior mode estimated by identifying the marker group with the largest number of markers amplified. Ties are labeled ambiguous.

True Type	Posterior Mode					
	CVF	MTB	SLV	BLD	SMN	Ambiguous
Cervical fluid	55	1	0	0	0	3
Menstrual blood	17	6	0	0	0	7
Saliva	0	0	80	0	0	0
Blood	0	0	0	65	0	0
Semen	0	0	0	0	86	0

APPENDIX B: DATA GENERATION

The body fluid samples used for this study were collected from voluntary donors with informed consent. DNA/RNA co-extraction, DNase treatment, reverse transcription, PCR amplification, PCR purification and detection for all mRNA analyses were executed based on protocols outlined in [Roeder and Haas \(2016\)](#), except an MSMB marker has been used instead KLK3. For some samples, the mRNA extraction protocol was modified to recover mRNA from EZ1 DNA investigator kit cartridges (Qiagen) post DNA extraction. Detection of marker amplification was performed by a 3500 Series Genetic Analyzer (ThermoFisher Scientific). The raw data produces continuous profiles recording the level of fluorescence detected measured in relative fluorescence units (rfu). The rfu values are an approximation of the quantity (number of PCR amplicons) of each mRNA marker that has been detected. The binarised profiles are obtained using marker-specific thresholds for peak detection, which means that a peak height measurement is converted to 1 if it is above the threshold and 0 otherwise. A minimum peak height threshold of 50 was used in addition to a marker-specific threshold, which was the average plus three standard deviations of the peak heights of that marker, rounded to whole numbers (reverse transcription negative samples were used for these calculations). These values were set so to minimize the chances of scoring “background” as a true body fluid peak.

All samples used have a single fluid-type.

APPENDIX C: CONNECTION TO NESTED DIRICHLET PROCESS

We provide further detail setting out the Biclustering Dirichlet Process (BDP) in contrast to the NoB-LoC model ([Lee et al., 2013](#)) and the Nested Dirichlet Process (NDP), following [Rodríguez, Dunson and Gelfand \(2012\)](#) and making explicit the DP elements, which were integrated out in our presentation in the text. In order to convey the connections of our method with NoB-LoC and NDP, we return to the simple setup of Section 4.2 and bicluster a single $N \times M$ matrix as a single unit, dropping the fluid-type and marker-group blocks. We further simplify the presentation of BDP by using the DP rather than the MDP as our building block, removing the constraint on the maximum number of clusters.

The NDP takes N “centres” each with M subjects and clusters the centres, then groups subjects within centre clusters. The NDP differs from BDP in that there is no notion of “columns,” so no specific relation between subject j in centre i and subject j in centre i' . In our setting, they are equal, as the same markers $j \in \mathcal{M}$ are measured for each profile $i \in N$. If two centres i, i' are in the same cluster in the NDP, then their parameters $(\theta_{i,j})$ and $(\theta_{i',j})$ are sampled from the same DP-realisation, so they *may be* equal, whereas in the BDP, if two centres are in the same bicluster of the BDP then their parameters *must be* equal, so $\theta_{i,j} = \theta_{i',j}$.

On the other hand, NoB-LoC is a biclustering model for a $N \times M$ matrix $\mathbf{X} = [x_{i,j}]_{i=1,\dots,N}^{j=1,\dots,M}$ and hence, does have an explicit notion of “columns.” NoB-LoC uses a zero enriched Pólya urn scheme, which permits an extra ‘inactive’ category in the row-partition and the column partitions nested therein. For clarity, we drop that feature in the explanations below (equivalent to sitting $\pi_0 = \pi_1 = 0$ in the original NoB-LoC description).

As in Section 4.2, $R = (R_1, \dots, R_K)$ is a partition of $\{1, \dots, N\}$ and for $r \in \{1, \dots, K\}$, we let $S_k = (S_{k,1}, \dots, S_{k,K_r})$ be a partition of $\{1, 2, \dots, M\}$. We take $\alpha > 0$, $\beta > 0$ and H a centering or “base” distribution on the parameter space of $\theta_{i,j}$, $(i, j) \in \mathcal{N} \times \mathcal{M}$. The generative model for θ in the NDP is

$$\begin{aligned} Q &\sim \text{DP}(\alpha, \text{DP}(\beta, H)), \\ G_i &\sim Q, \quad i = 1, \dots, N, \\ \theta_{ij} &\sim G_i, \quad j = 1, \dots, M, \end{aligned}$$

all jointly independent. The NDP can be rewritten in a way that highlights the relation to the BDP and NoB-LoC:

The generative model for θ in the NDP is

$$\begin{aligned} Q &\sim \text{DP}(\alpha, \text{DP}(\beta, H)) \\ G_i &\sim Q, \quad i = 1, \dots, N, \text{ with } G = (G_1, \dots, G_N) \\ \text{and } G &\rightarrow (R, G^*) \text{ with } R = (R_1, \dots, R_K) \text{ and } G^* = (G_1^*, \dots, G_K^*) \\ \theta_{i,j} &\sim G_{k_i}^*, \text{ for all } (i, j) \in \mathcal{N} \times \mathcal{M}, \text{ where } i \in R_{k_i} \text{ defines } k_i. \end{aligned}$$

We now unpack this generative model, following the presentation in [Rodríguez, Dunson and Gelfand \(2012\)](#). If

$$Q \sim \text{DP}(\alpha, \text{DP}(\beta, H))$$

is a realisation of a DP with base distribution $\text{DP}(\beta, H)$ then Q can be written

$$Q = \sum_{t \geq 1} w_t \delta_{Q_t^*},$$

where $w_t, t \geq 1$ are weights generated by a stick-breaking process and the atoms $\{Q_t^*\}_{t \geq 1}$ are iid realisations of $\text{DP}(\beta, H)$. A set of N independent samples $G_1, \dots, G_N \sim Q$ is a subset of the atoms of Q , and some of the G_i 's may be equal. We reparameterize (G_1, \dots, G_N) as (R, G^*) where R is a partition of $\{1, \dots, N\}$ and $G^* = (G_1^*, \dots, G_K^*)$ are the K distinct realisations appearing in (G_1, \dots, G_N) , with $G_i = G_{k_i}^*$ when $i \in R_{k_i}$.

Since G_k^* is an atom of Q , it is a realisation of $\text{DP}(\beta, H)$, so for $k = 1, \dots, K$,

$$G_k^* = \sum_{t \geq 1} w_{k,t} \delta_{\psi_{k,t}^*}$$

where $w_{k,t}$, $t \geq 1$ are stick breaking weights and $\psi_{k,t}^*$, $t \geq 1$ are iid realisations of H . The NDP now takes $\theta_{i,j} \sim G_k^*$ independently for each $i \in R_k$ and iid for $j = 1, \dots, M$. If $i, i' \in R_k$ are in the same cluster then $\theta_{i,j}$ and $\theta_{i',j}$ have the same sampling distribution $G_i = G_{i'} = G_k^*$, and so we can get $\theta_{i,j} = \theta_{i',j}$ if the same atom in G_k^* is selected. However, in the BDP we want $\theta_{i,j} = \theta_{i',j}$ whenever $i, i' \in S_k$, not just with positive probability, so we diverge at this point.

The corresponding generative models for NoB-LoC and the BDP can be written as follows.

The generative model for θ in NoB-LoC and the BDP is

$$Q \sim \text{DP}(\alpha, \text{DP}(\beta, H))$$

$$G_i \sim Q, \quad i = 1, \dots, N, \quad \text{with } G = (G_1, \dots, G_N)$$

and $G \rightarrow (R, G^*)$ with $R = (R_1, \dots, R_K)$ and $G^* = (G_1^*, \dots, G_K^*)$ giving the unique DP-realizations in G . Next,

$$\theta_{k,j} \sim G_k^*, \quad k = 1, \dots, K, \quad \text{with } \theta_k = (\theta_{k,1}, \dots, \theta_{k,M})$$

and $\theta_k \rightarrow (C_k, \theta_k^*)$ with $C_k = (C_{k,1}, \dots, C_{k,K_k})$ and $\theta_k^* = (\theta_{k,1}^*, \dots, \theta_{k,K_k}^*)$ giving the unique θ -values in θ . Finally, for $k = 1, \dots, K$ and each $i \in R_k$,

NoB-LoC: (1) for each $l = 1, \dots, K_k$, draw $p_{i,l} \stackrel{\text{iid}}{\sim} H$;

(2) for each $j \in C_{k,l}$, set $\theta_{i,j} = p_{i,l}$

BDP: for each $j \in C_{k,l}$, set $\theta_{i,j} = \theta_{k,l}^*$.

For each row cluster $k = 1, \dots, K$ in NoB-LoC and BDP, we sample a single set $\theta_k = (\theta_{k,1}, \dots, \theta_{k,M})$ of parameters $\theta_{k,j}^* \stackrel{\text{iid}}{\sim} G_k^*$, for $j = 1, \dots, M$ to define the nested column clusters $C_k = (C_{k,1}, \dots, C_{k,K_k})$. We reparameterize θ_k as (C_k, θ_k^*) , where $\theta_k^* = (\theta_{k,1}^*, \dots, \theta_{k,K_k}^*)$ are the unique entries in θ_k and $C_k = \{C_{k,1}, \dots, C_{k,K_k}\}$ is a partition of $\{1, \dots, M\}$ satisfying $\theta_{k,\ell}^* = \theta_{k,j}$ when $j \in C_{k,\ell}$. The following describes a key difference between NoB-LoC and BDP. For each $(i, j) \in \mathcal{N} \times \mathcal{M}$, in NoB-LoC, we set $\theta_{i,j} = p_{i,l}$ with $p_{i,l} \stackrel{\text{iid}}{\sim} H$, where $i \in R_k$ and $j \in C_{k,l}$, which means that, if $(i, j), (i', j') \in R_k \times C_{k,l}$, $\theta_{i,j} = \theta_{i',j'}$ only if $i = i'$, so we share parameters across columns in the same row but not across rows within a bicluster. On the other hand, in BDP, $\theta_{i,j} = \theta_{k,l}^*$, so parameters are shared across all rows and columns within a bicluster.

The induced marginal distributions

$$R \sim \text{CRP}(\alpha, \mathcal{N}),$$

$$C_k \sim \text{CRP}(\beta, \mathcal{M}), \quad k = 1, \dots, K,$$

are known, and $\theta_{k,\ell}^* \stackrel{\text{iid}}{\sim} H$ for each k and $\ell = 1, \dots, K_k$. We work directly with these marginal distributions in setting up the BDP, and hence Q and G^* are not needed.

APPENDIX D: EXAMPLE OF NOTATION FOR NESTED CLUSTERING

Examples of \mathbf{X}, θ and $f(k), g(l)$ -cell labels introduced in Section 4.3 are shown in Figure 6. This is an artificial example with just $F = 2$ fluid-types and $N_1 = N_2 = 10$ observations per type, simulated for the purpose of illustration. These are given for $F = 2$ fluid-types

$\mathcal{F} = \{1, 2\}$, and $N = 20$ profiles, $N_1 = 10$ with labels $\mathcal{N}_1 = \{1, \dots, 10\}$ for fluid-type $f = 1$ and $N_2 = 10$ with labels $\mathcal{N}_2 = \{11, \dots, 20\}$ for fluid type $f = 2$. There are $M = 10$ markers with $M_1 = 5$ with labels $\mathcal{M}_1 = \{1, \dots, 5\}$ targeting the first fluid type, and $M_2 = 5$ with labels $\mathcal{M}_2 = \{6, \dots, 10\}$ targeting the second fluid type.

Figure 6(a) shows a possible random realization of the biclusters. The row partitions in the first fluid-type are $R_1 = (R_{1(1)} = \{1, 4, 8, 9, 10\}, R_{1(2)} = \{2, 6, 7\}, R_{1(3)} = \{3, 5\})$, while in the second fluid-type $R_2 = (R_{2(1)} = \{11, 13, 15, 16\}, R_{2(2)} = \{12\}, R_{2(3)} = \{14, 17, 18, 19\}, R_{2(4)} = \{20\})$, resulting in $K_1 = 3$ and $K_2 = 4$. The column partitions in the first subtype $R_{1(1)}$ in the first fluid-type are, for \mathcal{M}_1 , $S_{1(1),1} = (S_{1(1),1(1)} = \{1, 3, 4, 5\}, S_{1(1),1(2)} = \{2\})$, giving $K_{1(1),1} = 2$, whereas for \mathcal{M}_2 , $S_{1(1),2} = (S_{1(1),2(1)} = \{6\}, S_{1(1),2(2)} = \{7, 10\}, S_{1(1),2(3)} = \{8, 9\})$, which means $K_{1(1),2} = 3$. The column partitions in the second subtype $R_{1(2)}$ in the first fluid-type are, for \mathcal{M}_1 , $S_{1(2),1} = (S_{1(2),1(1)} = \{1, 2, 5\}, S_{1(2),1(2)} = \{3, 4\})$, while for \mathcal{M}_2 , $S_{1(2),2} = (S_{1(2),2(1)} = \{6, 8, 9, 10\}, S_{1(2),2(2)} = \{7\})$, which gives $K_{1(2),1} = K_{1(2),2} = 2$. We omit column partitions in the third subtype of the first fluid type and the clusters for the second fluid-type. As an example of bicluster notation, the bicluster $C_{2(4),2(2)} = \{(20, 7), (20, 9), (20, 10)\}$ (the gray-blue bicluster in the bottom right block in (a)) has $c_{2(4),2(2)} = 3$ cells.

Figure 6(b) shows a possible random realization of the θ -values, given the biclustering. These are constant within $(f(k), g(l))$ clusters. For example all eight cells $(i, j) \in C_{2(1),2(2)}$ (the pink bicluster in the bottom right block of (a)) have $\theta_{i,j} = \theta_{2(1),2(2)}^* = 0.34$. Figure 6(c) shows a realisation of the $N \times M$ binary data-matrix \mathbf{X} . Each entry $x_{i,j}$ is an independent Bernoulli random variable with success probability $\theta_{i,j}$. The number of successes $s_{f(k),g(l)}$ in bicluster $(f(k), g(l)) = (2(1), 1(1))$ (the white bicluster in the bottom left block in (a)) is $s_{2(1),1(1)} = 4$.

APPENDIX E: CHOICE OF PRIOR HYPERPARAMETERS

In Section 4.3.4, the activation probabilities $\theta_{f(k),g(l)}^*$ in bicluster $(f(k), g(l)) \in \mathcal{C}_{f,g}$ were taken to have priors $\theta_{f(k),g(l)}^* \sim \text{Beta}(a_{f,g}, b_{f,g})$, $f, g \in F$ with potential different shape parameters in each of the 25 fluid-marker blocks $(f, g) \in \mathcal{F} \times \mathcal{F}$, which gives 50 prior hyperparameters there. We have a further twenty hyperparameters α_f, J_f and β_g, L_g for the MCRP distributions taken in Sections 4.3.1 and 4.3.2 respectively. We used the training data to assign these hyperparameters fixed values.

E.1. Prior row and column clustering hyperparameters. The number of columns in a marker group is small ($M_g = 5$ for $g = 1, 3, 4, 5$ and $M_2 = 7$), so we were not concerned about partitions with a long tail of small clusters and simply took $L_g = M_g$ (the number of columns in marker group g) with β_g chosen to give a prior probability $\pi(L_g = 1) \approx 0.5$ for all $g \in \mathcal{F}$, inducing $\beta_2 = 0.375$ and $\beta_g = 0.49$ for $g \neq 2$. Following simple exploratory work on the training data (k -means clustering of rows and visualization in Figure 1), we set the MCRP row parameter $J_f = 5$, $f \in \mathcal{F}$ to give a hard upper limit on the number of fluid subtypes equal five. Next, we select α_f separately for each $f \in \mathcal{F}$ to give a prior probability $\pi(\alpha_f \in \{1, 2\}) \approx 0.5$, (giving $\alpha_1 = 0.6025$, $\alpha_2 = 0.725$, $\alpha_3 = 0.55$, $\alpha_4 = 0.585$ and $\alpha_5 = 0.525$) as the N_f -values in Table 1 vary with $f \in \mathcal{F}$. A sensitivity analysis is performed with smaller and larger J -values in Appendix I.

E.2. Prior activation probability hyperparameters. Inspection of Figure 1 suggests that in blocks $(f, g) \in \mathcal{F} \times \mathcal{F}$ with $f = g$, suitable choices of $a_{f,g}$'s and $b_{f,g}$ may be $a_{f,f} = 1/2$ and $b_{f,f} = 1/4$ and $a_{f,g} = 1/2$ and $b_{f,g} = 1$ with $f \neq g$ for all $f, g \in \mathcal{F}$. By inspection, we observe general patterns among candidate biclusters. In the on-diagonal blocks

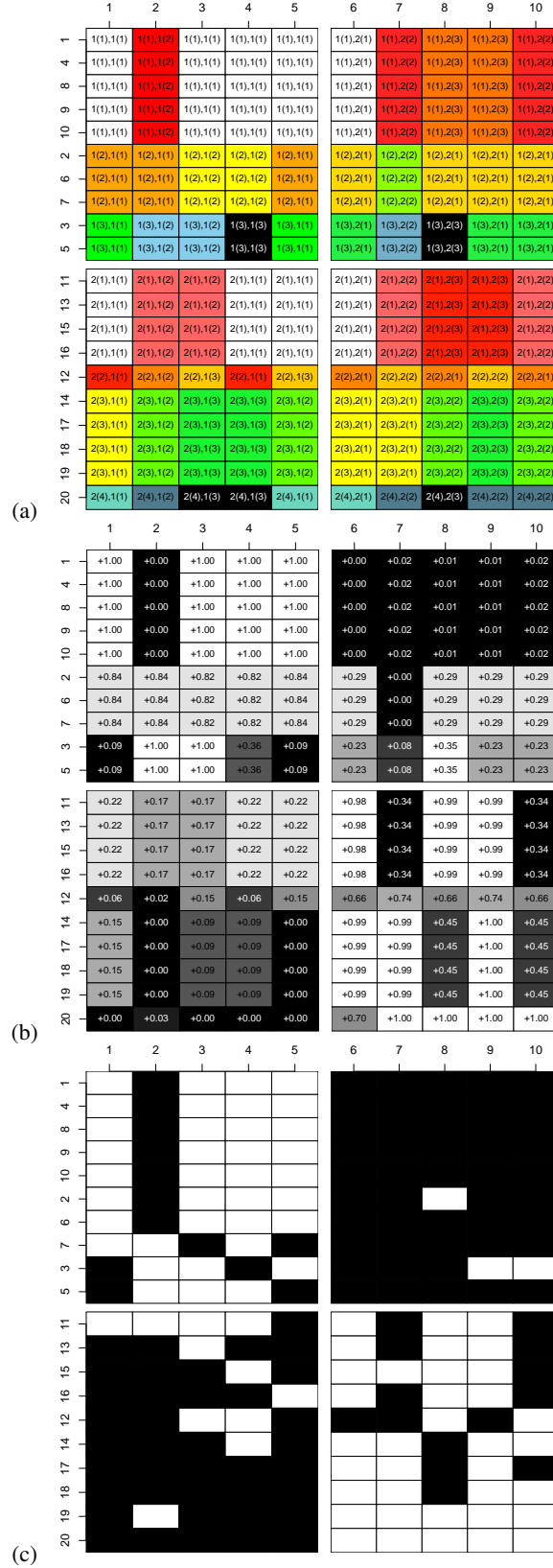


FIG 6. Simulated biclustering and simulated data: (a) Data matrix with simulated clustering labels $f(k), g(l)$ at cells $(i, j) \in C(f(k), g(l))$ (b) matrix of simulated cell success probabilities θ with the θ_{ij} value in each cell $(i, j) \in \mathcal{N} \times \mathcal{M}$; (c) simulated data, cells are white/black ($\mathbf{X}_{ij} = 1/0$) with probability θ_{ij} given in the corresponding cell middle.

(i.e., $f = g$), biclusters tend to be either completely active or inactive, while in the off-diagonal blocks (i.e., $f \neq g$), they tend to be inactive but noisier. However, exceptions seem warranted in the on-diagonal MTB/MTB and CVF/CVF blocks and the off-diagonal MTB/CVF and MTB/BLD blocks, where $a_{1,1} = b_{1,1} = 1$, $a_{2,2} = b_{2,2} = 1$, $a_{2,1} = b_{2,1} = 1$ and $a_{2,4} = b_{2,4} = 1$, respectively.

We checked (and slightly modified) these elicited values following MCMC simulations targeting $\pi(a_f, b_f, R_f | \mathbf{X}_f)$ (with $a_f = (a_{f,1}, \dots, a_{f,F})$ and $b = (b_{f,1}, \dots, b_{f,F})$) separately for each fluid-type, taking independent $\Gamma(0.01, 0.01)$ priors for all $a_{f,g}$ and $b_{f,g}$. Posterior mean parameter values are given in Table 6. We could of course use this in our overall anal-

Fluid-type	Marker group				
	CVF	MTB	SLV	BLD	SMN
CVF	(1.1, 0.5)	(0.5, 2.5)	(0.1, 0.9)	(0.1, 1.6)	(0.3, 1.0)
MTB	(1.8, 0.6)	(0.6, 1.0)	(0.8, 19)	(0.8, 0.9)	(0.4, 13)
SLV	(0.1, 0.5)	(0.3, 7)	(0.3, 0.1)	(1e-4, 4.5)	(0.8, 40)
BLD	(0.4, 43)	(0.1, 0.8)	(0.1, 10)	(0.4, 0.1)	(1e-3, 4.9)
SMN	(0.2, 15)	(0.4, 8.1)	(0.2, 3.5)	(0.2, 35)	(0.6, 0.2)

TABLE 6

The grid gives posterior mean values of prior parameters $(a_{f,g}, b_{f,g})$ for the $\text{Beta}(a_{f,g}, b_{f,g})$ -prior distributions for activation probabilities $\theta_{f(k),g(l)}^$ in biclusters $(f(k), g(l)) \in \mathcal{C}_{f,g}$ across the twenty five fluid-type/marker-group blocks $(f, g) \in \mathcal{F} \times \mathcal{F}$.*

ysis, but we found mixing rather slow (even on the smaller separate fluid-type data sets) and preferred to fix these hyperparameters. This choice was borne out by the well-calibrated posterior distributions we subsequently obtained for the test data in Section 8. All the training data in Table 1 were used for these a -and- b measurements and no test data and no unlabeled profiles, so $\mathcal{U} = \emptyset$ and $\mathcal{N}_f = \mathcal{T}_f$ here.

Marginal Highest Posterior Density (HPD) Bayesian Credible Intervals (BCI) for each of the eighteen off-diagonal blocks (excluding MTB/CVF and MTB/BLD) are given (on the original and log scales) in Figure 7. The horizontal red lines gives a -and- b values at $a_{f,g} = 0.174$ and $b_{f,g} = 0.807$. These are consensus values for all distributions except $a_{3,4}$ (SLV/BLD, 9'th BCI) and $a_{4,5}$ (BLD/SMN, 14'th BCI).

Since we expect more noise in the test data (and in real casework data) than in the training data we use slightly "less extreme" values than the training data suggest, especially for blocks such as BLD/SMN ($f = 4, g = 5$) and SLV/BLD ($f = 3, g = 4$), which with all marker signal absent in the training data. The chosen fixed values are given in Table 7, which are generally

Fluid-type	Marker group				
	CVF	MTB	SLV	BLD	SMN
CVF	(1, 1)	(0.2, 0.8)	(0.2, 0.8)	(0.2, 0.8)	(0.2, 0.8)
MTB	(1, 1)	(1, 1)	(0.2, 0.8)	(1, 1)	(0.2, 0.8)
SLV	(0.2, 0.8)	(0.2, 0.8)	(0.45, 0.15)	(0.2, 0.8)	(0.2, 0.8)
BLD	(0.2, 0.8)	(0.2, 0.8)	(0.2, 0.8)	(0.45, 0.15)	(0.2, 0.8)
SMN	(0.2, 0.8)	(0.2, 0.8)	(0.2, 0.8)	(0.2, 0.8)	(0.45, 0.15)

TABLE 7

The grid gives the elicited fixed values of the prior hyperparameters $(a_{f,g}, b_{f,g})$ for the $\text{Beta}(a_{f,g}, b_{f,g})$ -prior distributions for activation probabilities $\theta_{f(k),g(l)}^$ in biclusters $(f(k), g(l)) \in \mathcal{C}_{f,g}$ across the 25 fluid-type/marker-group blocks $(f, g) \in \mathcal{F} \times \mathcal{F}$.*

more conservative than the values in Table 6 would allow, but close to the consensus values from Figure 7 for off-diagonal blocks.

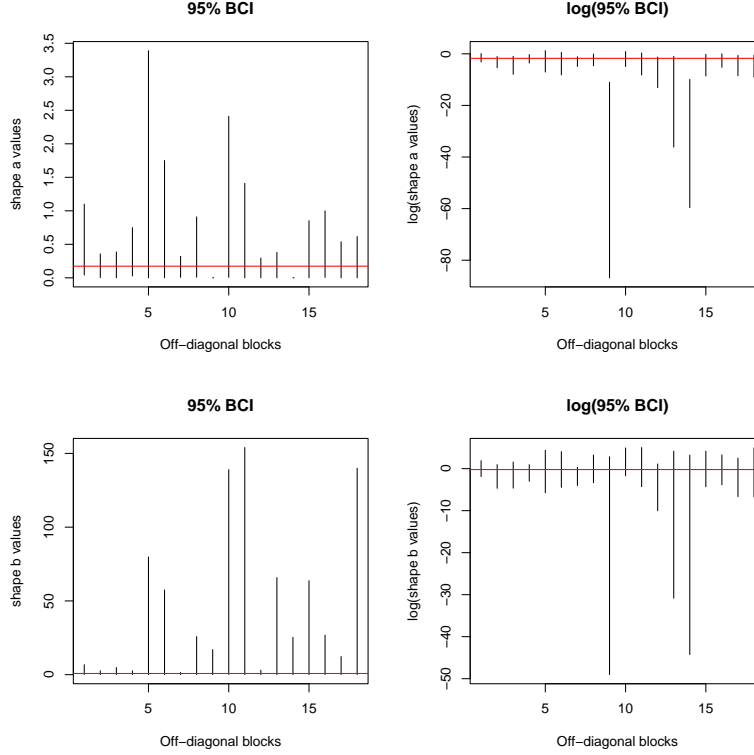


FIG 7. The graphs show 95% HPD Bayesian credible intervals for the shape parameters in each of the eighteen off-diagonal blocks excluding MTB/CVF and MTB/BLD. Left column shows a (top) and b (bottom) intervals, right column shows $\log(a)$ (top) and $\log(b)$ (bottom).

APPENDIX F: MCMC UPDATES

We describe the various proposal distributions used in the MCMC to sample the posterior distribution under the nested finite mixture model. These target $\pi(R|\mathbf{X}) = \prod_{f \in F} \pi(R_f|\mathbf{X}_f)$ for $R \in \Xi_{\mathcal{T}, \mathcal{U}}^*$, the posterior including unlabeled profiles in Section 5.3.2. Since the knowledge of R determines \mathcal{V} exactly, we can equivalently write the target $\pi(R, \mathcal{V}|\mathbf{X})$ for $\mathcal{V} \in \Psi_{\mathcal{U}}$ and $R \in \Xi_{\mathcal{T}, \mathcal{V}}^*$. For each proposal move, we first outline the general algorithm, followed by the mathematical details.

F.1. Sampling the subtype assignment with fixed fluid-type assignments.

F.1.1. Outline. A value $i \in \mathcal{N}$ is chosen uniformly at random. The set of potential subtypes consists of the existing subtypes, except the current subtype containing i . If the current number of subtypes is less than J and i does not form a singleton subtype, an empty subtype is added to the potential set of subtypes. A subtype is randomly selected from the potential set to be the proposed subtype, followed by accepting or rejecting this proposal based on the appropriate Metropolis-Hastings ratio.

F.1.2. Details. Assuming the current state of the chain is $R \in \Xi_{\mathcal{T}, \mathcal{V}}^*$ with fixed assignment partition \mathcal{V} , the subtype partition R_f for all $f \in \mathcal{F}$ is updated according to the following. We give the general setting (where for example, a fluid-type could have just one profile), so in practice, some of the “corner cases” we accommodate explicitly below will not arise on our data.

Firstly, we select at random $f \sim U(\mathcal{F} \setminus \mathcal{F}^{(1)})$, where $\mathcal{F}^{(1)} = \{\tilde{f} \in \mathcal{F} : N_{\tilde{f}} = 1\}$. This setup forbids updating subtypes within a fluid-type containing only a single mRNA profile, as it can only have one subtype. Then, we randomly draw an existing subtype $k \sim U\{1, \dots, K_f\}$, from which a profile $i \sim U(R_{f(k)})$.

Let $n_{f(k)} = |R_{f(k)}|$ give the number of mRNA profiles in $R_{f(k)}$. Suppose (Case A) that $R_{f(k)}$ is a singleton subtype, i.e., $R_{f(k)} = \{i\}$, and hence $n_{f(k)} = 1$. Select a new subtype $k' \sim U(\{1, \dots, K_f\} \setminus \{k\})$ of fluid-type f , so that $k' \neq k$. Subtype $f(k)$ will be removed if the move to the new subtype is accepted. Note that K_f must be at least two in Case A as we have a singleton and $N_f > 1$ so there is another profile and hence a subtype with $k' \neq k$. In other proposals (like Case B below), k' is chosen from a set including a new $K_f + 1$ subtype. That choice is not included in Case A, as it would be a pointless singleton-to-singleton move. Re-indexing the subtypes in fluid type f , we set

$$R'_{f(\ell)} = \begin{cases} R_{f(\ell)}, & \text{for } \ell \in \{1, \dots, k-1\} \\ R_{f(\ell+1)}, & \text{for } \ell \in \{k, \dots, K_f-1\} \end{cases}$$

Finally, we set $R'_{f(k')} \leftarrow R'_{f(k')} \cup \{r\}$, and hence the proposed subtype partition of fluid-type f is $R'_f = (R'_{f(1)}, \dots, R'_{f(K_f-1)})$. The proposal probability for this update is

$$q_A(R'_f | R_f) = \frac{1}{K_f(K_f - 1)}$$

If (Case B) $n_{f(k)} > 1$, then $R_{f(k)}$ is not a singleton subtype, so it remains non-empty after the removal of profile i . We randomly select a new subtype

$$k' \sim \begin{cases} U(\{1, \dots, K_f + 1\} \setminus \{k\}), & \text{if } K_f < J_f, \\ U(\{1, \dots, K_f\} \setminus \{k\}), & \text{if } K_f = J_f. \end{cases}$$

Again, the selection procedure ensures $k' \neq k$, and if $k' = K_f + 1$, then a new (singleton) will be created.

Suppose (Case B.1) $k' \leq K_f$, which means that the proposed subtype already exists, and the total number of subtypes of fluid-type k will not be changed by the update. The proposed subtype partition for fluid-type f is $R'_f = (R'_{f(1)}, \dots, R'_{f(K_f-1)})$, with

$$R'_{f(\ell)} = \begin{cases} R_{f(\ell)} \setminus \{r\} & \text{for } \ell = k, \\ R_{f(\ell)} \cup \{r\} & \text{for } \ell = k', \\ R_{f(\ell)} & \text{otherwise.} \end{cases}$$

On the other hand, if (Case B.2) $k' = K_f + 1$, resulting in a new subtype for the proposal, then proposed subtype partition for fluid-type f is $R'_f = R_f \cup \{R_{f(K_f+1)}\}$ with $R_{f(K_f+1)} = \{i\}$. These two updates induce the proposal probability

$$q_B(R'_f | R_f) = \begin{cases} \frac{1}{K_f^2 n_{f(k)}} & \text{for } K_f < J_f, \\ \frac{1}{K_f(K_f-1) n_{f(k)}} & \text{for } K_f = J_f. \end{cases}$$

Note that for Case B.2, we must have $K_f < J_f$.

Detailed balance holds between Case A and Case B.2. The acceptance probability for the proposed state R'_f in Case A is

$$\alpha_A(R'_f | R_f) = \begin{cases} 1, & \frac{\pi(R'_f | \mathbf{X}_f) q_B(R_f | R'_f)}{\pi(R_f | \mathbf{X}_f) q_A(R'_f | R_f)} \end{cases}$$

$$\begin{aligned}
&= \left\{ 1, \frac{\pi_R(R'_f) \prod_{\ell=1}^{K_f-1} p(\mathbf{X}_{f(\ell)} | R'_{f(\ell)}) K_f (K_f - 1)}{\pi_R(R_f) \prod_{\ell=1}^{K_f} p(\mathbf{X}_{f(\ell)} | R_{f(\ell)}) (K_f - 1)^2 (n_{f(k')} + 1)} \right\} \\
&= \left\{ 1, \frac{\pi_R(R'_f) p(\mathbf{X}_{f(k')} | R'_{f(k')}) K_f}{\pi_R(R_f) p(\mathbf{X}_{f(k')} | R_{f(k')}) p(\mathbf{X}_{f(k)} | R_{f(k)}) (K_f - 1) (n_{f(k')} + 1)} \right\}.
\end{aligned}$$

On the other hand, the acceptance probability for the proposed state R'_f for Case B.1 is

$$\alpha_{B.1}(R'_f | R_f) = \left\{ 1, \frac{\pi_R(R'_f) p(\mathbf{X}_{f(k')} | R'_{f(k')}) p(\mathbf{X}_{f(k)} | R'_{f(k)}) n_{f(k)}}{\pi_R(R_f) p(\mathbf{X}_{f(k')} | R_{f(k')}) p(\mathbf{X}_{f(k)} | R_{f(k)}) (n_{f(k')} + 1)} \right\},$$

while that for Case B.2 is

$$\alpha_{B.2}(R'_f | R_f) = \left\{ 1, \frac{\pi_R(R'_f) p(\mathbf{X}_{f(k')} | R'_{f(k')}) p(\mathbf{X}_{f(k)} | R'_{f(k)}) n_{f(k)} K_f}{\pi_R(R_f) p(\mathbf{X}_{f(k)} | R_{f(k)}) (K_f + 1)} \right\}.$$

Since \mathcal{V} is fixed, and independent MCRP is applied to the subtype clustering to each fluid-type $f \in \mathcal{F}$, these updates can be applied in parallel to target each $\pi(R_f | \mathbf{X}_f, \mathcal{V}_f)$, $f \in \mathcal{F}$ independently and sample $\pi(R | \mathbf{X}, \mathcal{V})$, $R \in \Xi_{\mathcal{T}, \mathcal{V}}^*$.

The following section provides an update on mixing over \mathcal{V} .

F.2. Metropolis-Hastings sampler for updates across fluid-types.

F.2.1. Outline. The index of an unlabeled type $i \in \mathcal{U}$ is selected uniformly at random. Uniformly choose a subtype $f' \in \mathcal{F}_{-i}$ at random, where $\mathcal{F}_{-i} = \mathcal{F} \setminus y_i, y_i \in \mathcal{F}$. We then randomly and uniformly select a subtype from the chosen type above. The potential subtypes include the existing subtypes in fluid-type f' , but also include an empty subtype if $|f'| < J$. The proposed fluid-type and subtype for i are accepted or rejected based on the appropriate Metropolis-Hastings ratio.

F.2.2. Details. Let $R \in \Xi_{\mathcal{T}, \mathcal{U}}^*$ be the current state of the Markov Chain. As remarked above, if R is given, then the corresponding \mathcal{V} is determined. We choose an unlabeled profile $i \sim U(\mathcal{U})$ at random, i.e., $i \in \{N + 1, \dots, N + U\}$. Suppose $i \in R_{f(k)}$ for some $k \in \{1, \dots, K_f\}$. Subsequently, we randomly select $f' \sim U(\mathcal{F} \setminus \{f\})$, draw

$$k' \sim \begin{cases} U\{1, \dots, K_{f'} + 1\} & \text{for } K_{f'} < J_{f'}, \\ U\{1, \dots, K_{f'}\} & \text{for } K_{f'} = J_{f'} \end{cases}$$

and remove i from $R_{f(k)}$ and add it in $R'_{f(k')}$. If $k' \leq K_{f'}$ then i is added to an existing subtype $R_{f(k')}$ of fluid-type f' , whereas if $k' = K_{f'} + 1$ then i forms a new subtype $R_{f(K_{f'}+1)} = \{i\}$.

If (Case A) $R_{f(k)} = \{i\}$, the update removes subtype $R_{f(k)}$ from fluid-type f , so the proposed partition for fluid-type f is $R'_f = \cup_{\tilde{k}=1}^{K'_f} \{R'_{f(\tilde{k})}\}$, where

$$R'_{f(\tilde{k})} = \begin{cases} R_{f(\tilde{k})} & \text{for } \tilde{k} \in \{1, \dots, k-1\}, \\ R_{f(\tilde{k}+1)} & \text{for } \tilde{k} \in \{k, \dots, K'_f = K_f - 1\}. \end{cases}$$

If (Case B) $n_{f(k)} > 1$, then $R_{f(k)}$ is not a singleton, so K_f remain unchanged and

$$R'_{f(\tilde{k})} = \begin{cases} R_{f(\tilde{k})} & \text{for } \tilde{k} \in \{1, \dots, K_f\} \setminus k, \\ R_{f(\tilde{k})} \setminus \{i\} & \text{for } \tilde{k} = k. \end{cases}$$

For both Cases A and B, if $k' = K_{f'} + 1$, implying $K_{f'} < J_{f'}$, then a new subtype is created in the proposed fluid-type f' . We obtain $R'_{f'} = \cup_{\tilde{k}=1}^{K_{f'}} \{R'_{f'(\tilde{k})}\}$ with

$$R'_{f'(\tilde{k})} = \begin{cases} R_{f'(\tilde{k})} & \text{for } \tilde{k} \in \{1, \dots, K_{f'}\}, \\ \{i\} & \text{for } \tilde{k} = K_{f'} = K_{f'} + 1. \end{cases}$$

On the other hand, if $k' \leq K_{f'}$, that is, the proposed subtype assignment already exists, then we have

$$R'_{f'(\tilde{k})} = \begin{cases} R_{f'(\tilde{k})} & \text{for } \tilde{k} \in \{1, \dots, K_{f'}\} \setminus k', \\ R_{f'(\tilde{k})} \cup \{i\} & \text{for } \tilde{k} = k', \end{cases}$$

which is permitted for $K_{f'} \leq J_{f'}$.

Depending on $K_{f'}$ only, the proposal probabilities are

$$q(R'|R) = \begin{cases} (U(F-1)(K_{f'}+1))^{-1} & \text{if } K_{f'} < J_{f'}, \\ (U(F-1)K_{f'})^{-1} & \text{if } K_{f'} = J_{f'}. \end{cases}$$

In Case A with $R_{f(k)} = \{i\}$, the Hasting's ratio $q(R|R')/q(R'|R)$ is

$$H_A(R'|R) = \begin{cases} \frac{K_{f'}+1}{K_f} & \text{if } K_{f'} < J_{f'}, \\ \frac{K_{f'}}{K_f} & \text{if } K_{f'} = J_{f'}. \end{cases}$$

When $n_{f(k)} > 1$, for Case B.1 with $K_f < J_f$, the Hasting's ratio is

$$H_{B.1}(R'|R) = \begin{cases} \frac{K_{f'}+1}{K_f+1} & \text{if } K_{f'} < J_{f'}, \\ \frac{K_{f'}}{K_f+1} & \text{if } K_{f'} = J_{f'}, \end{cases}$$

whereas for Case B.2 with $K_f = J_f$, the Hastings ratio is simply $H_{B.2}(R'|R) = H_A(R'|R)$.

F.3. Gibbs sampler for updates across fluid-types in the Cut-Model inference.

F.3.1. Outline. The Gibbs Sampler presented here is a special case of a Nested MCMC sampler. Nested MCMC for Cut-Models was suggested in [Plummer \(2015\)](#) and is described above in Section 6, where some of the following notation is introduced. Our sampler proposes a new partition by randomly selecting the fluid-type and subtype for an unlabeled profile i according to the full conditional probability $p(R'|R_{-i})$. Details below explain the sampling algorithm for classifying a single profile (SPC) and multiple profiles simultaneously (JPC).

F.3.2. Details. After obtaining $\pi(Q|\mathbf{X}_{\mathcal{T}})$ using MCMC and the sampler in Section F.1, for each $t = 1, \dots, T_0$, Gibbs sampling is employed to simulate a side chain from $\pi(R|\mathbf{X}, Q^{(t)})$. For the t th side chain, we first randomly select $R_0^{(t)}$, an initial state for the row partitions of $(\mathcal{T}, \mathcal{U})$, conditioned on $Q^{(t)}$ such that $R_0^{(t)} \in \Xi_{\mathcal{T}, \mathcal{U}}^*(Q^{(t)})$. Therefore, the initial joint partition $R_0^{(t)}$ of the labeled and unlabeled data contains the partition $Q^{(t)}$ of the labeled data as a joint sub-partition.

At step $t' = 1, \dots, T_1$ of this MCMC chain, we randomly select an unlabeled profile $i \sim U(\mathcal{U})$. Subsequently, we construct a Gibbs sampler to draw $R^{(t,t')} \in \Xi_{\mathcal{F}, \mathcal{U}}^*(Q^{(t)})$ from the full conditional distribution

$$R^{(t,t')} \sim \pi \left(\cdot | R_{-i}^{(t,t'-1)} \right),$$

which is equivalent to sampling the vector of probabilities with components given by

$$\Pr \left(i \in R_{f(k)}^{(t,t')} | R_{-i}^{(t,t'-1)} \right) \propto p \left(\mathbf{X} | R_{-i}^{(t,t'-1)}, i \in R_{f(k)}^{(t,t')} \right) \pi \left(R^{(t,t')} \right),$$

for $f \in \mathcal{F}$ and

$$k \in \begin{cases} \{1, \dots, K_f^{(t,t')} + 1\} & \text{if } K^{(t,t')} < J_f, \\ \{1, \dots, K_f^{(t,t')}\} & \text{if } K^{(t,t')} = J_f, \end{cases}$$

where $K_f^{(t,t')}$ is the number of subtypes in fluid-type $f \in \mathcal{F}$ in $R^{(t,t')}$. When the analyses are performed with SPC, $T_1 = 1$ is sufficient for all $t \in T_0$; in other words, a single draw by the Gibbs sampler is sufficient for each subchain. However, in the JPC analyses, for each proposal by the Gibbs sampler, we select an unlabeled profile $i \sim \text{Uniform}(\mathcal{U})$ at random and draw R' from $p(R' | R_{-i})$. In this case, length of each subchain T_1 is set such that each unlabeled profile $i \in \mathcal{U}$ would be updated ≥ 10 times on average.

F.4. Runtime, Convergence and Implementation Checks for Metropolis Hastings.

To get an idea of runtimes, in the best case, the Cut-Model setup estimating a fluid-type for a single profile, we get around 10 Effective Independent Samples per second (so 600 EIS'/minute) on a standard office desktop computer in a careful Java implementation, but without parallelization. This value is computed using the Effective Sample Size (ESS) for the fluid-type of the unlabeled profile and excludes the one-off cost of sampling subtypes for training data. In the worst case, Bayesian inference for joint estimation of fluid-type for our test set of 46 samples, which includes estimating the subtype structure for the 321 profiles in the training data, we obtain approximately 1.5 EIS'/minute, equivalently, roughly a half-day to get the joint fluid-type posterior for 46 profiles if we target an ESS equal 1000 for each profile. This is just representative, using a central ESS value among those we observed for sample fluid-type values $y_i = \{f : i \in \mathcal{V}_f\}$.

For convergence diagnostics, we focus on achieving large ESS values for the random fluid-type y_i of unlabeled samples $i \in \mathcal{U}$. Across all 740 MCMC runs for the different analyses in this paper (the majority being LOOCV checks on training data) an ESS well above 1000 seems typical. The ESS values and ranges for all the analyses are given in Table 8.

The implementation is checked by verifying our software reproduced the MCRP distributions when setting the log-likelihood function to return zero. We hand-checked likelihood calculations for a small number of profiles in a single subtype. Also, we performed classification on the unlabeled profile with all missing values and checked that the posterior distribution for its fluid-type was indeed uniform on \mathcal{F} . This is discussed further in Appendix G. Our LOOCV checks on the training data check correct (but blinded) classification of training data with known labels.

APPENDIX G: MISSING DATA AND UNBIASED FLUID-TYPE LABELLING

There are no missing marker values $x_{i,j}$, $i \in \mathcal{N}$, $j \in \mathcal{M}$ in the training and test data. However, if a profile did have missing marker values, then this is easy to handle as explained in Section 5.3.3: in the product over $(i, j) \in C(f(k), g(l))$ in Equation 8, we simply omit from the product any cells (i, j) for which the value of $x_{i,j}$ is missing.

TABLE 8

Range of the ESS of the mode type variable across all unlabelled profiles for each analysis. The mode type variable is coded in binary format, where 1 = yes and 0 = no. The ESS range is calculated excluding any unlabelled profiles with a mode type that has a posterior probability of 1.0. Below SPC and JPC stand for “Single” and “Joint” Profile Classification, respectively.

Analysis	ESS Median & Range	Purpose	Section
LOOCV on the training set in Bayesian inference	4500 (2772, 4500)	Evaluate goodness-of-fit, calibration and classification performance with Bayesian inference, using model and lab-quality data.	Section 8.3
LOOCV on the training set in Cut-Model inference	4500 (2412, 4500)	Evaluate goodness-of-fit, calibration and classification performance with Cut-Model inference, using model and lab-quality data, and compare to the corresponding Bayesian analysis.	
JPC of profiles in the test set in Bayesian inference	3955 (1672, 4500)	Evaluate the performance of the trained model for jointly classifying casework-like data using Bayesian inference and lab-quality training data.	Section 8.4
JPC of profiles in the test set in Cut-Model inference	4500 (2402, 4500)	Evaluate the performance of the trained model for jointly classifying casework-like data using Cut-Model inference and lab-quality training data, and compare to the corresponding Bayesian analysis.	
SPC of profiles in the test set in Bayesian inference	4500 (1313, 4500)	Evaluate the performance of the trained model for classifying casework-like data one at a time using Bayesian inference and lab-quality training data, and compare to the corresponding joint analysis.	
SPC of profiles in the test set in Cut-Model inference	4500 (936, 4500)	Evaluate the performance of the trained model for classifying casework-like data one at a time using Cut-Model inference, and lab-quality training data, and compare to the corresponding Bayesian analysis.	
JPC of profiles in the test set in Bayesian inference ($J_f = 1$ & $L_g = 1$)	4500 (3117, 4500)	To investigate the effect of cluster bounds on the classification of casework-like data.	Appendix I
JPC of profiles in the test set in Bayesian inference ($J_f = 1$ & $L_g = M_g$)	4500 (3496, 4500)		
JPC of profiles in the test set in Bayesian inference ($J_f = 10$ & $L_g = M_g$)	3703 (1856, 4500)		
JPC of profiles in the test set in Bayesian inference ($J_f = 15$ & $L_g = M_g$)	3765 (1277, 4500)		

The prior $\pi_{\mathcal{V}}(\mathcal{V}) = F^{-U}$ on the fluid-type assignment partition \mathcal{V} of unlabeled profiles, presented in Section 5.3.2, takes the prior for the fluid-type of each unlabeled profile to be independent of the fluid-types of other unlabeled profiles and uniform on \mathcal{F} . However, it may be of concern that the labeled training data somehow distort this and changes the prior weighting, perhaps because the number of training profiles varies from one fluid-type to another, and the number of subtypes is upper-bounded. We formalize this by considering the

posterior distribution of \mathcal{V} when *all* the data x_i , $i \in \mathcal{U}$ are missing: when $\mathbf{X}_{\mathcal{U}}$ provides no information about the fluid-types of unlabeled profiles we require $\pi(\mathcal{V}|\mathbf{X}_{\mathcal{T}}, \mathbf{X}_{\mathcal{U}}) = F^{-U}$.

A joint partition $R \in \Xi_{\mathcal{T}, \mathcal{U}}^*$ of all profiles specifies the assignment \mathcal{V} of unlabeled profiles to fluid-types. However, it contains more information as each unlabeled profile $i \in \mathcal{V}_f$ is assigned some subtype $k \in \{1, \dots, K_f\}$, so $i \in R_{f(k)}$. Let $Q(R)$ be the joint partition on training profiles, defined in Section 6, which we get by removing all the floating profiles from R .

Consider the likelihood $p(\mathbf{X}|R)$ in Equation 16 with $\mathbf{X} = (\mathbf{X}_{\mathcal{T}}, \mathbf{X}_{\mathcal{U}})$. In this case, with all $\mathbf{X}_{\mathcal{U}}$ missing, the entries in $\mathbf{X}_{\mathcal{U}}$ do not contribute to c and s in Equation 9. Consequently, the likelihood is the probability for $\mathbf{X}_{\mathcal{T}}$ only, and this depends only on the joint partition Q of the labeled profiles. It follows that

$$p(\mathbf{X}|R) = p(\mathbf{X}_{\mathcal{T}}|Q),$$

where $Q = Q(R)$ as in a Cut-Model.

The outcome $\{Q, \mathcal{V}\}$ occurs iff $R \in \mathbf{X}_{\mathcal{T}, \mathcal{V}}^*(Q)$ occurs, where $\mathbf{X}_{\mathcal{T}, \mathcal{V}}^*(Q)$, defined in Equation 17, is the set of joint partitions R that contain Q and assign unlabeled profiles to fluid-types according to \mathcal{V} . We have

$$\begin{aligned} \pi(Q, \mathcal{V}|\mathbf{X}) &\propto \sum_{R \in \mathbf{X}_{\mathcal{T}, \mathcal{V}}^*(Q)} p(\mathbf{X}|R) \pi_R(R) \\ &= p(\mathbf{X}_{\mathcal{T}}|Q) \sum_{R \in \mathbf{X}_{\mathcal{T}, \mathcal{V}}^*(Q)} \pi_R(R) \\ &= p(\mathbf{X}_{\mathcal{T}}|Q) \pi_{Q, \mathcal{V}}(Q, \mathcal{V}), \end{aligned}$$

with $\pi_{Q, \mathcal{V}}(Q, \mathcal{V}) = \pi_Q(Q) \pi_{\mathcal{V}}(\mathcal{V})$, so $\pi(\mathcal{V}|\mathbf{X}) = \pi_{\mathcal{V}}(\mathcal{V}) = F^{-U}$. This result is intuitive: no data, no classification. The same property, $\pi_{cut}(\mathcal{V}|\mathbf{X}) = \pi_{\mathcal{V}}(\mathcal{V})$, holds in the Cut model case. We used this property to check our code.

The acceptance probabilities for move type $T \in \{A, B.1, B.2\}$ are

$$\alpha_T(R'|R) = \min \left\{ 1, \frac{\pi(R'|X)}{\pi(R|X)} H_T(R'|R) \right\}.$$

There is quite a bit of cancellation in the acceptance probability. Our implementation always works with the full sum of log-likelihoods across a fluid-type, but in this sum, only the log-likelihoods of subtypes that change in the update are themselves updated. This is the time-limiting step and is handled efficiently.

APPENDIX H: RESULTS

In section 8.3, Figure 3 summarises the results of the LOOCV of the Bayesian analysis on the training set. For LOOCV of the Cut-Model analysis on the training dataset, the summary in the same style is presented in Figure 8, which conveys a very similar message as Figure 3, in particular, the confusion tables (bottom right panel) are identical in both figures. The choice of the inference framework, Bayes or Cut-Model, does not influence the results of interest or our conclusion on the classification.

Confusion tables for the classification of the test data using the fluid-type of the posterior mode in SPC and JPC analyses (identical for Bayes and Cut-Model analyses) are given in Table 9. The only differences are observed in the classification of two mRNA profiles: a CVF sample with an inconclusive \log_{10} BF for a CVF label < 1 across all four analyses; an SMN profile with \log_{10} BF for an SMN label equal 1.054 for Bayesian JPC, but less than one in the other three analyses, so right on the borderline.

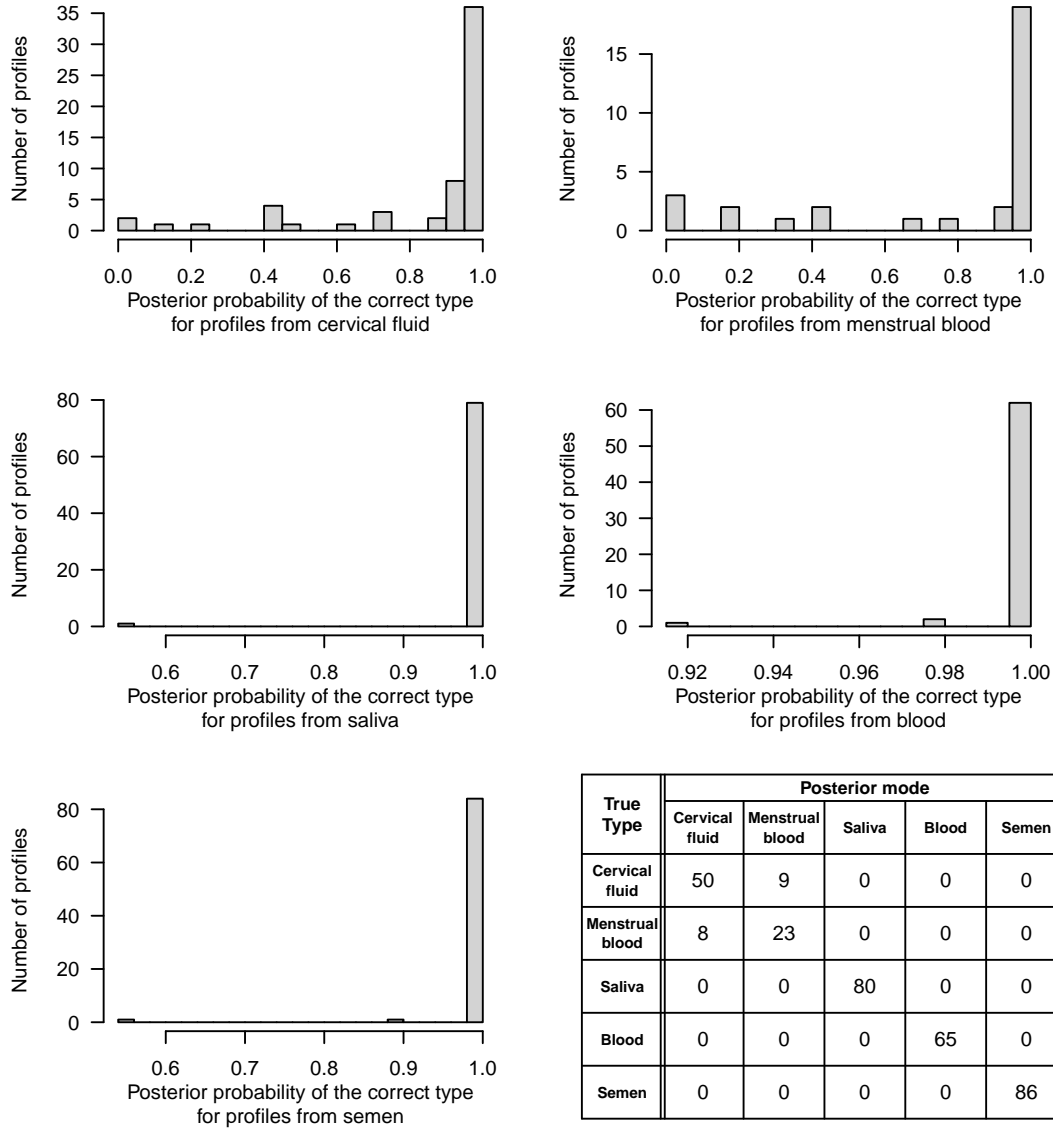


FIG 8. Posterior mode probability and mode of the correct type (for mRNA profiles in the training set) estimated from the LOOCV analysis on the training data with Cut-Model inference. This is discussed in Section 8.3.

APPENDIX I: SENSITIVITY ANALYSIS FOR BOUNDS ON PARTITION COUNT.

Figure 9 presents the comparisons in the estimated posterior probabilities of the correct types for the mRNA profiles in the test set between the default model ($J_f = 5, L_g = M_g$) and other choices of J_f . Given a (J_f, L_g) combination, the results are very similar between Bayesian and Cut-Model inferences.

From panels (a)–(d) of Figure 9, there appears to be greater dispersion in the posterior probabilities of the true types for $(J_f = 1, L_g = 1)$ and $(J_f = 1, L_g = M_g)$ than the default model. The dispersion appears to be strong for $(J_f = 1, L_g = 1)$. This suggests that the posterior probabilities are poorly calibrated when we do not accommodate the heterogeneity within a fluid-type and the variation in the marker amplification within a group (within a fluid-type). Panels (e)–(h) of Figure 9 show that there is generally close agreement in the

TABLE 9

The posterior mode estimated across the samples of the test set by SPC and JPC (identical for both Bayesian- and Cut-Model inference).

True Type	Posterior Mode									
	One at a Time (SPC)					Joint (JPC)				
	CVF	MTB	SLV	BLD	SMN	CVF	MTB	SLV	BLD	SMN
Cervical fluid	23	1	0	0	0	22	2	0	0	0
Menstrual blood	0	0	0	0	0	0	0	0	0	0
Saliva	0	0	10	0	0	0	0	10	0	0
Blood	0	0	0	2	0	0	0	0	2	0
Semen	1	0	0	0	9	0	0	0	0	10

posterior probabilities of the true types between the default model and $(J_f = 10, L_g = M_g)$, and between the default model and $(J_f = 15, L_g = M_g)$. These results do not depend on the choice of the inference framework.

FIG 9. Comparing the estimated posterior probabilities of the correct types of the mRNA profiles in the test set between the default model ($J_f = 5, L_g = M_g \forall f, g \in \mathcal{F}$) and other choices of J_f and L_g . Each panel in the left columns is a comparison between two analyses in the Bayesian framework, while each in the right is in the Cut-Model framework. For legibility, the positions on axes are in logit-space, while the labels represent the corresponding probability values.

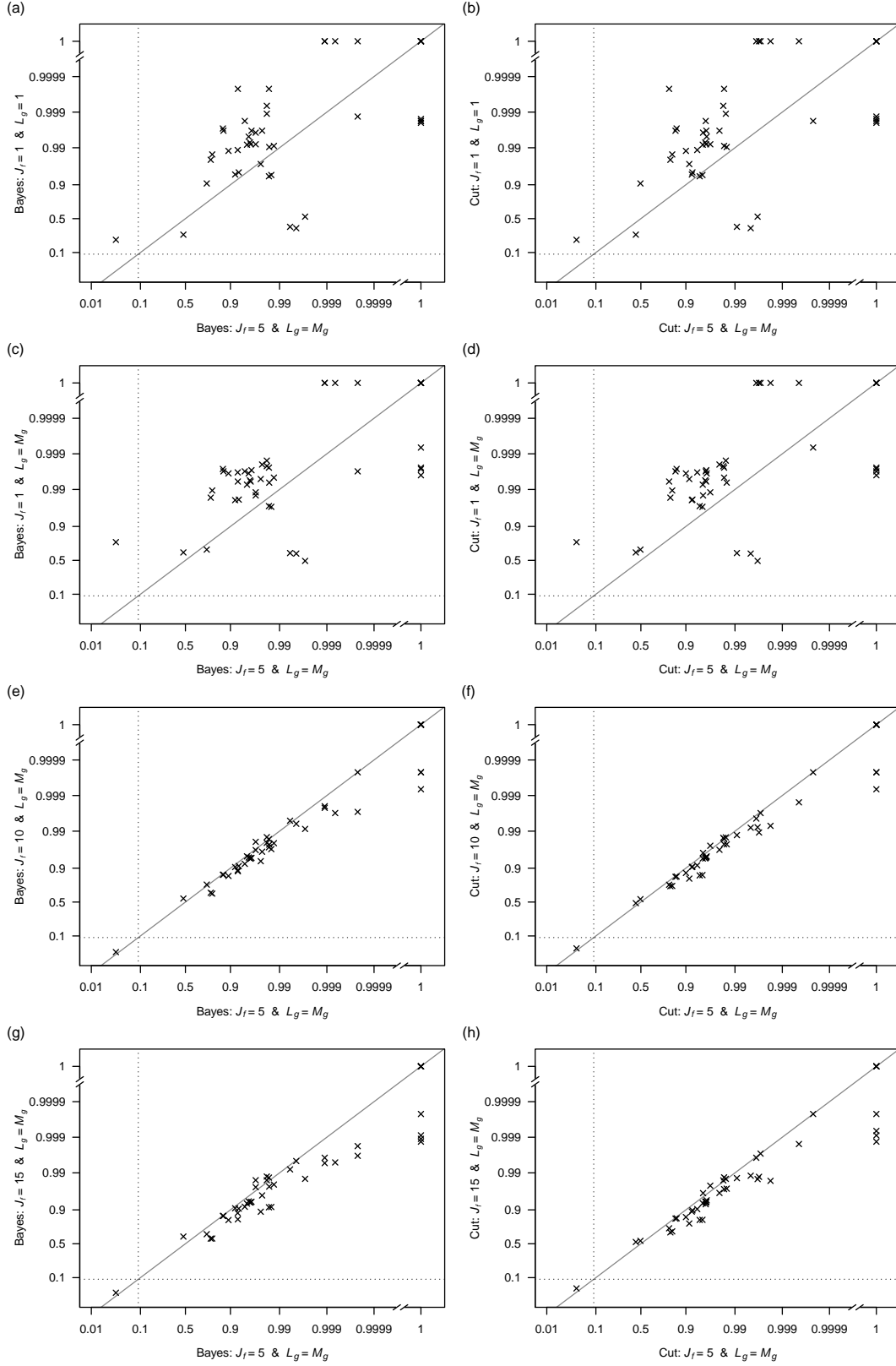


FIG 10. Posterior distribution of the number of subtypes within each fluid-type. Each panel in the left columns is a comparison between two analyses in the Bayesian framework, while each in the right is in the Cut-Model framework.

